Title

Conserved metabolite regulation of stress granule assembly via AdoMet

Journal

Journal of Cell Biology, 219(8)

ISSN

0021-9525

Authors

Begovich, Kyle
Vu, Anthony Q
Yeo, Gene
et al.

Publication Date

2020-08-03

DOI

10.1083/jcb.201904141

Peer reviewed

JCB Journal of Cell Biology

ARTICLE

Conserved metabolite regulation of stress granule assembly via AdoMet

Kyle Begovich[1,2], Anthony Q. Vu[3,4,5], Gene Yeo[3,4,5], and James E. Wilhelm[1,2]

Stress granules (SGs) are evolutionarily conserved condensates of ribonucleoproteins that assemble in response to metabolic stresses. Because aberrant SG formation is associated with amyotrophic lateral sclerosis (ALS), understanding the connection between metabolic activity and SG composition can provide therapeutic insights into neurodegeneration. Here, we identify 17 metabolic enzymes recruited to yeast SGs in response to physiological growth stress. Furthermore, the product of one of these enzymes, AdoMet, is a regulator of SG assembly and composition. Decreases in AdoMet levels increase SG formation, while chronic elevation of AdoMet produces SG remnants lacking proteins associated with the 5′ end of transcripts. Interestingly, acute elevation of AdoMet blocks SG formation in yeast and motor neurons. Treatment of ALS-derived motor neurons with AdoMet also suppresses the formation of TDP-43–positive SGs, a hallmark of ALS. Together, these results argue that AdoMet is an evolutionarily conserved regulator of SG composition and assembly with therapeutic potential in neurodegeneration.

Introduction

Cells deploy a variety of mechanisms to fine-tune biochemical processes in response to environmental stressors. One of these mechanisms is the formation of stress granules (SGs), evolutionarily conserved, cytoplasmic condensates comprising nontranslating mRNPs (Panas et al., 2016; Protter and Parker, 2016). SGs assemble in response to a variety of nutrient and metabolic stresses and are believed to provide a mechanism for coupling metabolic stress to posttranscriptional gene regulation (Kedersha et al., 2002; Khong et al., 2017; Panas et al., 2016; Protter and Parker, 2016). Furthermore, SGs act as centers to regulate cell signaling outputs and protein folding, highlighting SGs as global integrators of the stress response (Arimoto et al., 2008; Harding et al., 2000; Kedersha et al., 2013; Wippich et al., 2013). SGs are transient and require tight regulation of both assembly and disassembly for cell function and viability. Consistent with this, disruption of SG formation decreases cell survival when the stress is removed (Eisinger-Mathason et al., 2008; Kim et al., 2012; Kwon et al., 2007; Orrù et al., 2016; Yang et al., 2014).

In addition to their role in integrating the cellular stress response, SGs have been implicated in a variety of neurodegenerative disorders. Mutations in the SG components FUS (fused in sarcoma) and HNRNPA2B1, as well as TARDBP (encoding transactive response DNA binding protein 43 kD [TDP-43]) have been linked to amyotrophic lateral sclerosis (ALS) and frontotemporal dementia (FTD; Kim et al., 2013; Kwiatkowski et al., 2009; Martinez et al., 2016; Sreedharan et al., 2008; Vance et al., 2009). Interestingly, pathogenic mutations in these genes all cluster in regions that encode low-complexity sequences (LCSs) or intrinsically disordered regions (IDRs; Chen-Plotkin et al., 2010; Ryan et al., 2018; Shang and Huang, 2016). These pathogenic IDR and LCS domains drive recruitment of the proteins into SGs and alter the dynamics and composition of SGs that form in response to the altered protein (Decker et al., 2007; Gilks et al., 2004; Kato et al., 2012; Kim et al., 2013; Ling et al., 2013; Murakami et al., 2015; Patel et al., 2015; Protter et al., 2018; Ryan et al., 2018). Consequently, dysregulation in SG dynamics in ALS patients results in accumulation of atypical cytoplasmic, SG-like protein aggregates in dying neurons of the brain and spinal cord. Furthermore, accumulation of cytoplasmic TDP-43 in aberrant motor neuron (MN) SGs is considered a hallmark of ALS (Bentmann et al., 2012; Blokhuis et al., 2013; Farg et al., 2013; Keller et al., 2012; Kim et al., 2013; Liu-Yesucevitz et al., 2010). These results argue that understanding how SGs assemble in response to metabolic or nutrient stresses is critical for both understanding the pathophysiology of ALS and FTD and

[1]Howard Hughes Medical Institute, Summer Institute Marine Biological Laboratory, Woods Hole, MA; [2]Division of Biological Sciences, University of California, San Diego, La Jolla, CA; [3]Department of Cellular and Molecular Medicine University of California, San Diego, La Jolla, CA; [4]Stem Cell Program, University of California, San Diego, La Jolla, CA; [5]Institute for Genomic Medicine, University of California, San Diego, La Jolla, CA.

Correspondence to James E. Wilhelm: jwilhelm@ucsd.edu.

developing treatment strategies focused on disrupting the formation of aberrant SGs.

The current model for SG formation is that cellular stresses promote liquid–liquid phase separation (LLPS) of mRNPs via different multivalent interactions (Banani et al., 2017; Jain et al., 2016; Van Treeck et al., 2018; Wheeler et al., 2016). For instance, stress-induced disassociation of polysomes from translating mRNAs is thought to create a scaffold that can drive LLPS in two complementary ways (Panas et al., 2016; Protter and Parker, 2016). First, the exposure of sequences within the mRNA allows RNA–RNA interactions to help drive LLPS. Additionally, the recruitment of proteins with IDRs or LCSs to the exposed transcript can drive LLPS via protein–protein interactions. Together, these two mechanisms can greatly increase the number of mRNP interaction sites driving LLPS and SG formation. Consistent with this model, alterations in the protein levels of SG components, posttranslational modifications within IDRs, or LCSs of SG proteins regulate both protein–protein interactions and SG assembly (Hilliker et al., 2011; Hofweber et al., 2018; Swisher and Parker, 2010; Tsai et al., 2016, 2017).

Given the linkage between SGs and several neurodegenerative diseases, the composition of the SG proteome has been a subject of intense focus to identify potential therapeutic targets. Unfortunately, large-scale biochemical studies have found that SG composition is not only stress specific, but also organismal and cell type specific (Jain et al., 2016; Markmiller et al., 2018). Furthermore, these studies also revealed that SGs contain two distinct phases: a solid-like core and a dynamic surrounding shell (Jain et al., 2016; Markmiller et al., 2018). Although different mass spectrometry techniques have helped identify which components reside within each phase, the relative role of SG core proteins and shell proteins in SG formation and pathogenesis remains unclear.

Despite the fact that SG formation and composition is stress specific, there has been surprisingly little exploration of the connections between metabolism and SG assembly. To date, only a few metabolic enzymes have been shown to be enriched or localized to SGs via proteomic and/or targeted studies (Jain et al., 2016; Noree et al., 2019; Saad et al., 2017). This deficit is likely due to the limited number of stress conditions that have been used in SG proteomic studies. Interestingly, the localization of one metabolic enzyme, pyruvate kinase (Cdc19), to SGs has been shown to be crucial for reactivation of growth-promoting pathways upon removal of stress (Grignaschi et al., 2018; Saad et al., 2017). This suggests that SGs can play a critical role in regulating metabolic enzymes in response to stress. There are also limited examples of the reverse mode of regulation: metabolic intermediates that modulate SG assembly. Whereas SGs can assemble upon the removal of glucose or amino acids (Aguilera-Gomez et al., 2017; Reineke et al., 2018), only one metabolite from intermediate metabolism, acetyl-CoA, has been implicated in regulating SG formation (Rollins et al., 2017). Thus, the identification of metabolic enzymes that are recruited to SGs in a stress-specific manner would identify new linkages between SG formation and metabolism as well as provide a novel set of potential therapeutic targets for ALS and FTD.

Here, we have identified 17 metabolic enzymes that are recruited to yeast SGs in a stress-specific manner. Interestingly, *S*-adenosylmethionine (AdoMet), the product of one these enzymes, is a regulator of SG assembly and composition. The regulation of yeast SG formation by AdoMet is biphasic, with chronic changes altering SG composition and acute elevation of AdoMet suppressing SG assembly. Additionally, acute elevation of AdoMet suppresses SG formation in MNs, demonstrating conserved metabolite regulation of SG assembly from yeast to humans. The suppressive effect of AdoMet on SG formation also occurs in induced pluripotent stem cell (iPSC)-derived MNs from ALS patients. Most provocatively, AdoMet blocks the recruitment of cytoplasmic TDP-43 to remnant SGs in this cell culture model of ALS, implying that AdoMet can modify the pathogenic accumulation of SG material. Together, these results argue that metabolic activity controls both the composition and extent of SG formation and provide a framework for the identification of lead compounds that can modify or suppress SG formation.

Results

A subset of metabolic enzymes preferentially localize to SGs

Although SGs are known to assemble in response to a variety of nutrient and metabolic stresses, little is known how metabolic activity is linked to SG formation. That a number of metabolic enzymes self-organize into structures under conditions that also trigger the formation of SGs and processing bodies (P-bodies) suggests that the assembly of metabolic structures and RNA granules could be connected (Narayanaswamy et al., 2009; Noree et al., 2010, 2019). Consistent with this, three metabolic enzymes in the de novo purine biosynthetic pathway were recently discovered to localize to SGs upon growth to stationary phase (Noree et al., 2019). To explore the extent of metabolic enzyme recruitment to SGs, we screened all 34 known metabolic enzymes that form cytoplasmic foci for recruitment to SGs and/or P-bodies. Each metabolic enzyme was endogenously tagged with GFP, and the extent of enzyme recruitment to RNA granules was assayed at either 1 or 5 d of growth using Ded1-mCherry (SG marker) or Edc3-mCherry (processing-body [P-body] marker) expressed from its endogenous locus (Fig. 1). This screen identified 17 new metabolic enzymes that exhibited >15% colocalization with either type of RNA granule (Fig. 1 and Table S1). Whereas all 17 enzymes preferentially localized to SGs compared with P-bodies, 3 enzymes (Gly1, Gre3, and Pro3) were also enriched in P-bodies. Of the 17 enzymes we identified, 4 enzymes (Cdc19, Cys4, Sam1, and Sam2) were also found to be enriched in SGs from previous proteomic and targeted studies (Table S2 and Table S3; Jain et al., 2016; Saad et al., 2017). These results significantly broaden the number of metabolic enzymes recruited to SGs beyond those identified by prior proteomic and targeted studies (Table S2 and Table S3).

Our screen also revealed two distinct patterns of SG recruitment. 10 metabolic enzymes (Ade16, Ade17, Ald6, Gdh1, Gly1, Gre3, Hem13, Sam1, Sam2, and Pro3) were recruited directly to SGs. However, seven enzymes (Cdc19, Cys4, Dph2, Hem2, Imd3, Shm2, and Tpi1) had the ability to form structures independent of SGs, suggesting that this class of enzymes might form structures that are in turn recruited to SGs. Consistent

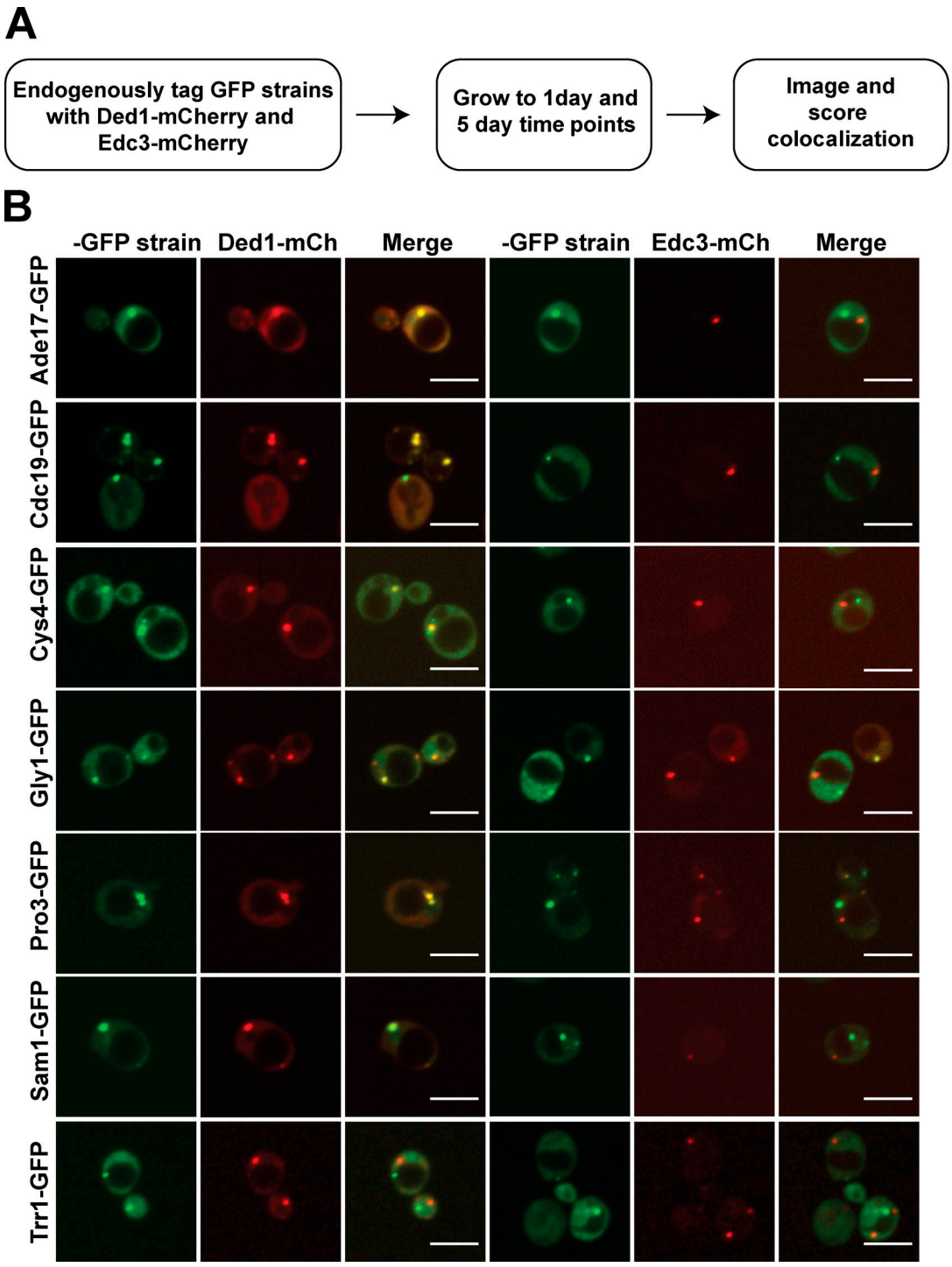

Figure 1. **Metabolic enzymes localize to RNA granules during late growth stages. (A)** Illustration of workflow for RNA granule screen. **(B)** Representative fluorescence images of endogenously expressed GFP-tagged metabolic enzymes and mCherry-tagged Ded1 (SGs) or Edc3 (P-bodies) from either 1-d (Ade17-GFP, Cdc19-GFP, Cys4-GFP, Sam1-GFP) or 5-d (Gly1-GFP, Pro3-GFP, Trr1-GFP) time points. Scale bar is 5 µm.

with this interpretation, enzymes in this class such as Cys4 and Cdc19 show a decline in the number of SG-independent structures at 5 d of growth compared with 1 d, as the number of cells with SGs increases on this time scale (Table S1).

Because RNA granules are enriched in proteins with IDRs and LCSs (Decker et al., 2007; Jain et al., 2016; Kato et al., 2012), we also examined whether any of these motifs were present and/or enriched in either class of SG associated metabolic enzymes. 12 of the 17 enzymes localized to SGs were predicted to contain an IDR and/or LCS; however, these motifs were found at an equal frequency among the 17 enzymes in our screen that were not recruited to RNA granules (Table S2 and Table S3). Thus, neither the ability to be recruited to a SG nor the pattern of recruitment can be predicted by the presence or absence of IDRs or LCSs.

Furthermore, only five of our SG associated enzymes have been annotated as having RNA binding activity by high-throughput screens (Table S2) implying that the majority of these enzymes are not recruited to SGs via RNA. Together, these results suggest that recruitment of metabolic enzymes to RNA granules occurs via novel, uncharacterized mechanisms.

The metabolic enzyme Sam1 is a stress-specific component of SGs

Recruiting metabolic enzymes to SGs represents potential way to couple SG assembly to changes in metabolic activity/stress. If this were the case, one might expect that the recruitment of metabolic enzymes to SGs would be stress specific. While our screen focused on standard growth stresses, including growth to postdiauxic shift (1 d) or growth to stationary phase (5 d) in rich medium, most studies of SGs focus on the effects of acute energy stresses on log-phase cells. This raised the possibility that this set of metabolic enzymes had been missed in prior studies of SGs because their recruitment is stress specific. To test this possibility, we examined whether one of the enzymes identified in our screen, *S*-adenosylmethionine synthetase 1 (Sam1; Figs. 1 B and 2, A and B), is recruited to SGs in response to acute energy stresses. In addition to its high degree of colocalization with SGs, we chose to focus on Sam1 because its substrates and products (methionine, ATP, and AdoMet) are highly used and connected to multiple metabolic pathways. Whereas Ded1-positive SGs readily formed in log-phase yeast that were treated with sodium azide or ethanol or shifted to medium lacking glucose, Sam1-GFP remained diffuse under all of these conditions (Fig. 2, C and D). It is worth noting that proteomic studies of the yeast SG identified Sam1 as a component of SGs that form in response to sodium azide (Jain et al., 2016). Thus, although Sam1 is not localized or enriched in SGs above background in our visual assay, it could still be present in SGs.

Because all of these stresses were acute energy stresses, we also tested the effects of translational stress on Sam1 recruitment to SGs. Given the role of methionine in translation initiation, we reasoned that acute methionine limitation may also trigger SG assembly. Sam1 catalyzes the ATP-dependent conversion of methionine to AdoMet (Fig. 2 A); thus, methionine limitation might be expected to both trigger SG assembly and regulate Sam1 activity and/or recruitment to SGs. Whereas shifting log-phase yeast to medium lacking methionine robustly triggered the assembly of Ded1-containing SGs, the SGs did not accumulate Sam1 above background levels (Fig. 2, C and D). Thus, methionine limitation constitutes a previously unidentified trigger for SG assembly; however, it is not a trigger for Sam1 enrichment in SGs.

Given these results, we next explored whether we could bypass the stress-specific recruitment of SGs by manipulating the levels of SG components. Overexpression of particular SG components can nucleate SG assembly in the absence of an external stress (Hilliker et al., 2011; Swisher and Parker, 2010). For instance, overexpression of either Ded1 or Pbp1 triggers the assembly of SGs in unstressed log-phase cells (Fig. 2, E and F). However, these SGs are not enriched in Sam1. Thus, merely triggering the aggregation of SG proteins is insufficient to recruit Sam1. Because Sam1 has a short LCS motif typical of SG nucleators, we also tested whether overexpression of Sam1 could trigger SG assembly. Overexpression of Sam1 in log-phase yeast did not cause protein aggregation or trigger SG formation (Fig. 2, E and F). Thus, Sam1 does not have a high propensity to aggregate in vivo. Consistent with this, we also found that Sam1 was recruited to only 30% of SGs formed in response to heat shock, while the majority of the protein remained diffuse (Fig. 2, G–I). Together, these results argue Sam1 is a stress-specific component of SGs, but it is not capable of nucleating SGs on its own.

Decreased levels of AdoMet trigger SG assembly and Sam1 recruitment

The stress-specific localization of Sam1 to SGs suggested that the products of Sam1 might play a role in modulating SG assembly. To test this possibility, we leveraged previous structure function studies of the *Escherichia coli* orthologue of Sam1, MetK, to design a set of mutations that disrupts the enzyme's activity (Taylor and Markham, 1999, 2000). Although each mutation resulted in a decrease in enzymatic activity of MetK, we used mutants that would disrupt enzyme tetramerization (C91Y) or ATP hydrolysis (D121N) or have no additional effect (K252M; Fig. S1 A). Each mutation was introduced into the endogenous *SAM1* locus and assayed for its effects on SG formation.

All three *SAM1*-inactivating mutations caused a threefold increase the assembly of SGs that were positive for two SG markers (Ded1 and Pbp1) and three metabolic enzymes (Sam1, Sam2, and Ade17; Fig. 3 A). Interestingly, both the C91Y and K252M mutations displayed no defects in Sam1 recruitment, while the ATP hydrolysis mutant, D121N, significantly reduced Sam1 localization to SGs (Fig. S1, B and C). Sam2's recruitment to SGs was also disrupted in the *SAM1* D121N allele, whereas Ade17, Ded1, and Pbp1 remained unaffected (Fig. S1, D and E). These results argue that the inactivation of Sam1, rather than disruption of its localization to SGs, is responsible for the increase in SG formation observed in all three *SAM1* mutations.

A potential way for Sam1 to regulate SG assembly would be to alter the levels of various SG components. Although the effects of Sam1 inactivation on Sam1 protein levels are allele dependent, all three *SAM1* mutations caused an ∼2.5-fold increase in Ded1 levels and a two- to fourfold increase in Sam2 protein, but had no effect on Ade17 levels (Fig. 3, B and C). However, this increase in Ded1 protein levels was not due to transcriptional upregulation (Fig. 3 D). Because overexpression of Ded1 can trigger SG assembly during log phase, this result suggested that one of the ways that Sam1 activity controls SG formation is via posttranscriptional regulation of Ded1 levels at growth to 1 d.

One way that the levels of the SG nucleator, Ded1, could be coupled to Sam1 activity is via the levels of AdoMet. To test this possibility, we first sought to determine if intracellular AdoMet levels were reduced in the *SAM1* D121N allele. Consistent with our prediction, AdoMet levels were reduced by ∼50% when *SAM1* D121N allele was grown for 24 h (Fig. S2 A). Next, if this were the case, exogenous AdoMet would be predicted to restore the SG formation in *SAM1* mutations to WT levels. To test this, we supplemented cultures of WT and mutant *SAM1* strains with

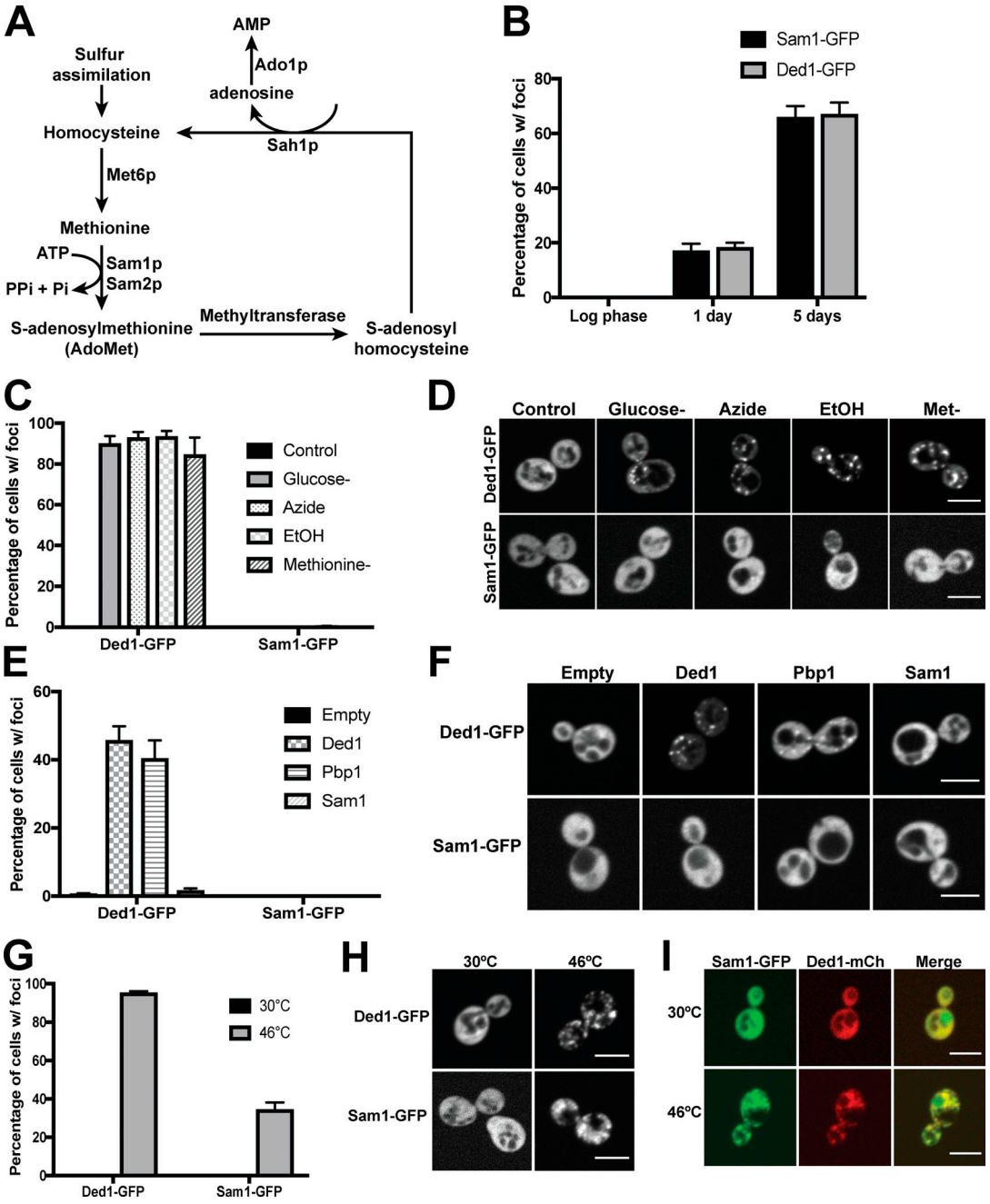

Figure 2. **Recruitment of Sam1 to SGs is stress specific. (A)** Diagram of methionine biosynthesis/recycling pathway in *S. cerevisae*. **(B)** Percentage of cells with Sam1-GFP foci and Ded1-GFP foci at different growth stages. Data are presented as average ± SEM of three independent replicates. **(C)** Percentage of logarithmically growing cells that form Ded1-GFP or Sam1-GFP foci upon exposure to different acute stresses. **(D)** Representative fluorescence images from C. **(E)** Percentage of logarithmically growing cells that form Ded1-GFP or Sam1-GFP foci in response to overexpression of SG nucleator proteins (Ded1 or Pbp1) or Sam1. **(F)** Representative fluorescence images from E. **(G)** Percentage of logarithmically growing cells that form Ded1-GFP or Sam1-GFP foci after a 10-min heat shock at 46°C. **(H)** Representative fluorescence images from G. **(I)** Representative fluorescence images of Sam1 colocalization with SGs (Ded1) under heat shock conditions. Bar graphs in C, E, and G are presented as average ± SEM of three individual replicates. Scale bars in D, F, H, and I are 5 µm.

250 µM AdoMet and assayed its effects on SG formation and Ded1 protein levels when grown for 24 h. In WT strains, exogenous AdoMet had no effect on the expression level of Ded1 or the frequency of SG formation, as indicated by Sam1-GFP and Ded1-mCherry (Fig. 3, E and F). In contrast, AdoMet treatment increased intracellular levels of AdoMet, restoring both protein levels of Ded1 and the frequency of SG formation to WT levels for all three *SAM1* loss-of-function mutations (Fig. 3, E and F; and Fig. S2 A). These results argue that decreases in AdoMet likely increase SG formation by elevating Ded1 protein levels.

Prolonged AdoMet accumulation disrupts SG assembly

AdoMet regulates SG accumulation under the same growth stress that triggers the recruitment of Sam1. This suggested that

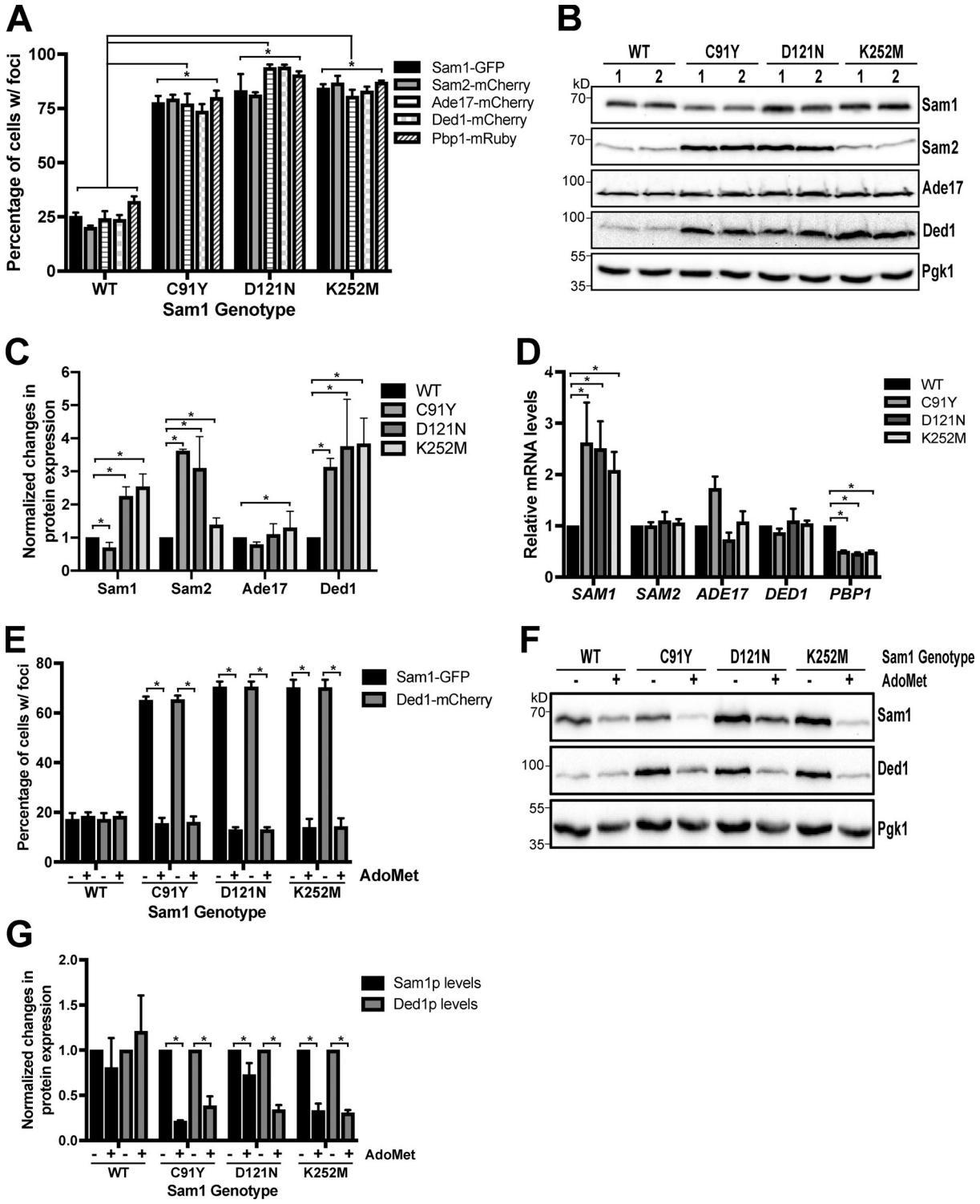

Figure 3. **Decreased AdoMet levels result in increased SG formation. (A)** Percentage of cells forming foci in strains endogenously expressing either mutant or WT Sam1-GFP with RFP-tagged metabolic enzymes (Sam2, Ade17) and SG markers (Ded1, Pbp1) in 1-d cultures. **(B)** Western blot analysis from strains used in A at 1-d time point. Numbers below each mutant indicate clone number for that genotype. **(C)** Quantification of proteins levels from B. Protein expression for each protein is normalized to the WT sample. **(D)** Quantification of mRNA levels using qPCR analysis from WT and mutant Sam1 alleles. **(E)** Percentage of cells forming foci in strains supplemented with 250 µM AdoMet and endogenously expressed WT or mutant Sam1-GFP alleles and Ded1-mCherry at 1-d growth. **(F)** Western blot analysis from strains used in E at 1-d time point. **(G)** Quantification of proteins levels from E. Protein expression is normalized to non–AdoMet-treated Sam1 and Ded1 within their respective genotype. Bar graphs in A, C–E, and G are presented as average ± SEM of three independent replicates. Pgk1 was used as a loading control in B and F. Statistical significance in A, C–E, and G was determined by one-tailed paired Student's *t* test (*, $P < 0.05$).

AdoMet might have an autoregulatory role in SG assembly when cells are grown under chronic nutrient stress. If this were true, one would expect that increases in AdoMet levels might block or greatly reduce SG formation at growth to 1 d. However, because AdoMet uptake is glucose dependent, our ability to increase AdoMet levels above normal is limited at the 1-d time point. As a result, we applied a genetic approach to manipulating AdoMet levels. Deletion of *ADO1* has been previously found to increase AdoMet levels by sevenfold at 1 d of growth compared with WT (Kanai et al., 2013). This suggested that deletion of *ADO1* might suppress SG formation. Consistent with this, deleting *ADO1* resulted in an approximately sixfold increase in AdoMet concentration and almost completely blocked the formation of Ded1-containing SGs at 1 d of growth (Fig. 4 A and Fig. S2 A).

One potential mechanism for the effect of *ado1Δ* on SGs is that increasing AdoMet levels at this time point decreases Ded1 expression. Consistent with this interpretation, we found that deletion of *ADO1* decreases protein levels of Ded1 by 70% (Fig. 4, B and C). Furthermore, the decrease in Ded1 protein levels occurred despite *DED1* mRNA levels increasing by 50% in *ado1Δ* strains (Fig. 4 D). Consistent with transcript levels from Sam1 inactivation strains, this argues that the effect of AdoMet on Ded1 expression is posttranscriptional. Additionally, even though Ded1 is a substrate for arginine methyltransferase, Hmt1, the posttranscriptional effects we observe are not mediated by Hmt1 or its target residues in Ded1, implying that these effects occur via a novel AdoMet-controlled pathway (Erce et al., 2013; Low et al., 2013; Fig. S3, A and B).

The striking effect of elevated AdoMet levels on Ded1 expression raised the possibility that AdoMet might be regulating composition and/or levels of multiple RNA granule components at growth to 1 d. To test this possibility, we examined the effects of *ado1Δ* on the localization of two P-body markers, Edc3 and Dcp2, as well as five additional SG proteins, eIF4E, eIF4G1, Pab1, Pbp1, and Pub1. Deletion of *ADO1* had no effect on P-body formation (Fig. S3, C and D). Thus, *ado1Δ* strains do not have a generalized defect in RNA granule assembly. In contrast to its effect on P-bodies, *ado1Δ* had selective effects on the recruitment of proteins to SGs. Pab1, Pbp1, and Pub1 were all recruited normally into SGs in the *ado1Δ* strain (Fig. 4 A). Thus, *ado1Δ*-mediated down-regulation of Ded1 does not eliminate SGs completely. In contrast, *ado1Δ* largely blocked the recruitment of eIF4E and eIF4G1 to SGs (Fig. 4 A). Interestingly, eIF4G1 protein levels were reduced by 50% in the *ado1Δ* strain, whereas eIF4E exhibited only a mild 10% reduction in protein expression (Fig. 4, B and C). Thus, *ado1Δ* down-regulates two components of SGs and blocks the recruitment of a third component, eIF4E.

If Sam1 participated in a feedback loop regulating SG assembly at growth to 1 d, one might expect that alterations in AdoMet levels would regulate Sam1 recruitment to SGs. To test this possibility, we examined the localization of four metabolic enzymes (Sam1, Ade17, Cdc19, and Cys4) in an *ado1Δ* strain background. Sam1 and Ade17 both failed to form foci when *ADO1* was deleted (Fig. S3 E). In contrast, Cdc19 and Cys4 both formed foci at normal levels. Unlike Ded1, the amount of all four proteins were either unchanged or elevated by the deletion of *ADO1* (Fig. S3, F and G). Furthermore, Cdc19 and Cys4 foci both colocalized with Pbp1-mRuby in *ado1Δ* strains, indicating that the structures are SG remnants (Fig. S3, H–K). Thus, AdoMet levels regulate the recruitment of a subset of metabolic enzymes to SG at growth to 1 d, including the enzyme that synthesizes AdoMet, Sam1.

AdoMet supplementation suppresses acute stress-induced SG assembly

Because the recruitment of metabolic enzymes to SGs is specific to growth to 1 d, we next investigated whether deleting *ADO1* had effects on the assembly of SGs regardless of the stress. Shifting yeast to medium lacking glucose, treatment with sodium azide, or heat shock, all triggered Ded1-SG assembly at the same frequency in WT and *ado1Δ* strains (Fig. 4, E and F). The failure of *ado1Δ* to suppress SG assembly during log phase was surprising, since AdoMet levels increased 50% during log phase (Fig. S2 B). This suggested that either the effect of AdoMet on SG assembly might be stress specific and have no effect on acute stress-induced SGs or this increase in AdoMet levels might not be sufficient to reduce SG formation under these conditions. To explore the second possibility, we grew WT yeast in medium supplemented with 250 µM AdoMet and then treated them azide. AdoMet treatment caused a reduction in the both the percentage of cells with foci and the number of foci per cell, as assayed with four different SG markers, Ded1, eIF4G1, Pab1, and Pub1 (Fig. 5, A–C). Intracellular AdoMet levels were significantly higher in AdoMet-supplemented cultures compared with untreated WT and *ado1Δ* strain (Fig. S2 B). Interestingly, unlike the effects we observed in *ado1Δ* strains, AdoMet treatment had no effect on the protein level of Ded1 or the other SG proteins we used as markers (Fig. 5 D). Shorter incubations with AdoMet were also effective. Treating cells for either 30 or 60 min with AdoMet before stress resulted in a significant reduction in SG formation, whereas a 15-min incubation failed to suppress SG formation (Fig. S4 C). Additionally, AdoMet-mediated SG suppression was not dependent on Hmt1 arginine methylation (Fig. 5, E–G). This suggests that AdoMet plays a critical role in suppressing SG assembly independent of protein levels or arginine methylation.

AdoMet's ability to suppress azide-induced SGs raised the question of whether it could suppress SG assembly in response to other canonical stresses. Shifting AdoMet-supplemented cultures to medium lacking glucose prevented SG assembly (Fig. S4 A). However, we observed no difference in heat shock–induced SGs when cultures were grown with exogenous AdoMet (Fig. S4 B). Thus, while AdoMet treatment suppresses SGs that form in response to acute energy stress, heat shock–induced SG assembly occurs via a different pathway.

One possible way that AdoMet might suppress SG assembly is via an effect on translation. Many of the stresses that trigger SG formation are thought to act via decreases in translation (Panas et al., 2016; Protter and Parker, 2016). This decrease in translation, in turn, leads to transcript release from polysomes enabling trans RNA–RNA, RNA–protein, and protein–protein interactions to nucleate SGs. This release step is believed to be critical for SG formation, since treatment with cycloheximide can prevent SG formation (Wheeler et al., 2016). If AdoMet acted

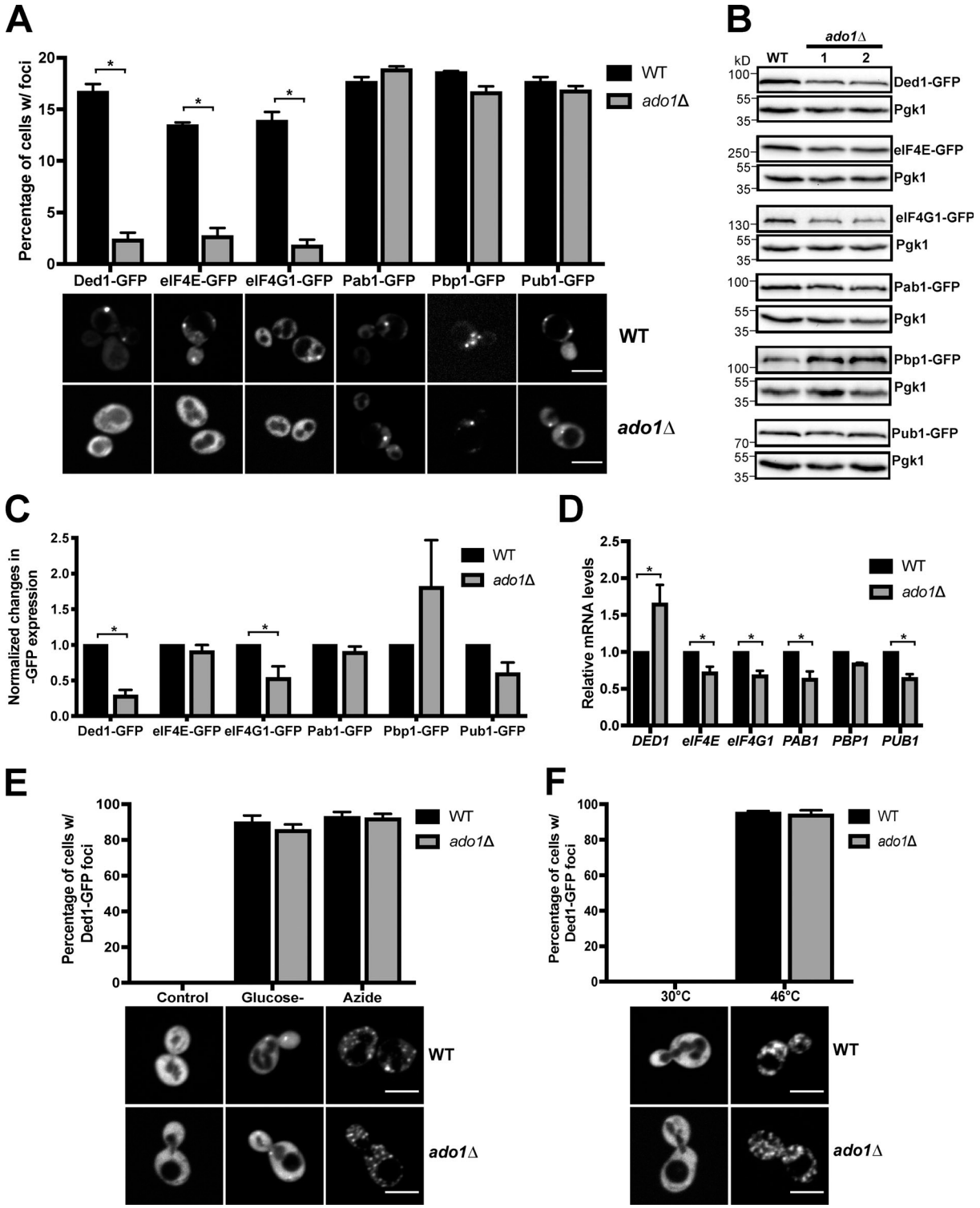

Figure 4. **5′ UTR mRNA-associated SG proteins are not recruited to SGs under high AdoMet levels under growth to 1 d. (A)** Quantification and representative fluorescence images of endogenously expressed GFP-tagged SG proteins in WT and *ado1Δ* strains at 1-d time point. **(B)** Western blot analysis of strains used in A at 1-d time point. Numbers below each mutant indicate clone number for that genotype. Pgk1 was used as a loading control. **(C)** Quantification of proteins levels from B. Protein expression for each protein is normalized to the WT sample. **(D)** Quantification of mRNA levels in WT and *ado1Δ* strains using qPCR analysis. **(E)** Quantification and representative fluorescence images of endogenously expressed Ded1-GFP in logarithmically growing WT and *ado1Δ* strains subjected to acute stress. **(F)** Quantification and representative fluorescence images of endogenously expressed Ded1-GFP in logarithmically growing WT and *ado1Δ* strains subjected to heat shock. Bar graphs in A and C–F are presented as average ± SEM of three independent replicates. Scale bars in A, E, and F are 5 µm. Statistical significance in A, C, and D was determined by one-tailed paired Student's *t* test (*, $P < 0.05$).

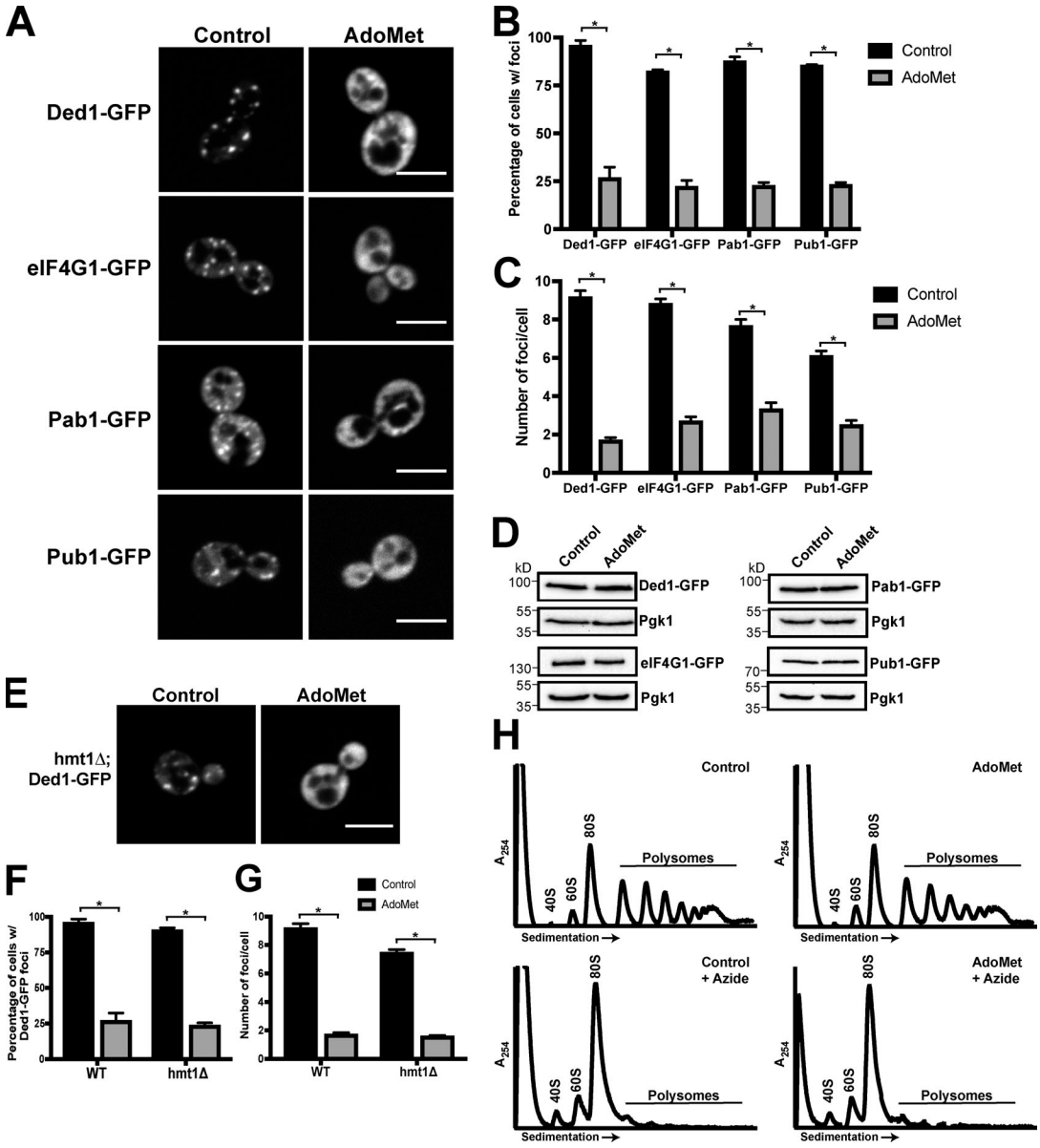

Figure 5. **Exogenous AdoMet suppresses acute stress-induced SGs. (A)** Representative fluorescence images of endogenously expressing GFP-tagged SG proteins upon azide treatment after growing logarithmically in the presence or absence of 250 µM AdoMet. **(B)** Quantification of cells with foci from A. **(C)** Quantification of the number of foci/cells from A. **(D)** Western blot analysis from strains used in A. **(E)** Representative fluorescence images of endogenously expressed Ded1-GFP in WT and *hmt1Δ* strains upon azide treatment. Pgk1 serves as a loading control. **(F)** Quantification of cells with foci from E. **(G)** Quantification of the number of foci/cell from E. **(H)** Polysome traces from cultures that were subjected to azide treatment after growing logarithmically in the presence or absence of 250 µM AdoMet. Bar graphs in B, C, F, and G are presented as average ± SEM of three independent replicates. Scale bars in A and E are 5 µm. Statistical significance in B, C, F, and G was determined by one-tailed paired Student's *t* test (*, P < 0.05).

at the level of translation, we would predict that polysome traces would still be intact in AdoMet-supplemented cultures when cells are exposed to azide. However, polysomes are absent in both azide-treated cells and cells that were grown with AdoMet before azide treatment (Fig. 5 H). AdoMet was also unable to relieve translational repression in glucose-starved cells, highlighting that this effect is not stress specific (Fig. S4 D). Thus, AdoMet plays a role in regulating SG assembly downstream of the inhibition of translation. Together, these results argue that AdoMet has two distinct effects on yeast SGs: an acute effect that suppresses SG formation and a late growth-stage effect that alters the expression of Ded1 and the recruitment of a subset of SG proteins.

AdoMet affects SG fusion in cultured mammalian cells

While AdoMet is an abundant, conserved metabolite, the assembly pathway for SGs differs between yeast and mammalian cells. Yeast SGs assemble via accretion/enlargement of an initial nucleation event (Wheeler et al., 2016). In contrast, mammalian SGs form via the fusion of many small SGs (Ivanov et al., 2003). This difference in dynamics suggested that the regulation of SG assembly by AdoMet might be specific to yeast. Because there is

no known stationary phase–like stress that can induce SGs in mammalian cells, we tested effects of AdoMet on SGs that form in response to acute stress. Pretreatment of either HeLa or U2OS cells with 4 mM AdoMet before oxidative stress with 500 µM sodium arsenite caused a shift from a small number of large SGs (–AdoMet) to a large number of small SGs (+AdoMet; Fig. 6, A, B, D, and E). Although shorter pretreatments with AdoMet affected SG formation in both HeLa and U2OS cells, the extent of the effect differed between the cell types. 15-, 30-, and 60-min pretreatment of HeLa cells with AdoMet before arsenite stress caused an increase in the number of small SGs in HeLa cells, with the maximal effect at 30 min (Fig. S5 A). In contrast to a longer AdoMet incubation, pretreatment of U2OS cells with AdoMet for 30 or 60 min before oxidative stress reduced the number of cells with SGs (Fig. S5 B), whereas a 3-h AdoMet incubation did not affect the number of cells with SGs. AdoMet treatment had no effect on the expression level of either G3BP1 or DDX3 in HeLa cells, arguing that the changes we observed in this cell line are not secondary to global changes in the levels of SG components (Fig. 6 C). Thus, AdoMet regulates SG assembly in both yeast and mammalian cells.

Because the composition of mammalian SGs varies depending on the type of stress and the cell type, we next explored whether AdoMet affected the dynamics of SGs that form in response to proteotoxic stress (MG132; Mazroui et al., 2007) or translational stress (rocaglamide [RocA]; Aulas et al., 2017). Pretreatment of HeLa cells with AdoMet caused an increase in SG number and a decrease in SG size for both proteotoxic and translational stress (Fig. 6, A and B). Thus, AdoMet pretreatment has the same effect on SG formation in HeLa cells for all three stresses we have tested. In contrast, AdoMet treatment decreases the percentage of U2OS cells that form SGs in response to the translational inhibitor, RocA, by approximately fourfold (Fig. 6, D and F). Because MG132 was unable to induce SGs in U2OS cells, we were unable to assay the effect of AdoMet on proteotoxic stress in these cells (data not shown). These results argue that cell type differences might modulate both SG formation and the response to AdoMet. Additionally, our results in HeLa cells suggest that AdoMet treatment disrupts a step in SG formation that is common to several different stress conditions.

That the AdoMet treatment caused many small SGs to form in response to a variety of stresses suggested that AdoMet treatment might be disrupting the fusion step in SG formation. If this were the case, the number and size of SGs would be relatively constant throughout the duration of the stress for AdoMet-pretreated cells, whereas in untreated cells, the number of SGs would fall as the SGs become larger owing to SG fusion. As predicted, the number of SGs decreased in untreated cells over the course of 1 h after arsenite treatment, whereas the number of SGs in AdoMet-treated cells remained largely constant (Fig. 7 A). Similarly, in untreated cells, we observed that the average size of SGs increased 1 h after arsenite treatment. In contrast, the average size of SGs in AdoMet-treated cells remained largely constant (Fig. 7 B). Although these results are consistent with AdoMet treatment altering the dynamics of SG fusion, it is also possible that AdoMet treatment might be buffering the oxidative stress due to arsenite. If this were the case, we would expect AdoMet treatment to decrease eIF2a phosphorylation after arsenite treatment. However, AdoMet treatment has no effect on the extent of eIF2a phosphorylation, implying that AdoMet is not buffering oxidative stress or disrupting the earliest steps in SG formation (Fig. 7, C and D). Together, these results argue that AdoMet treatment disrupts the fusion step of mammalian SG formation in HeLa cells.

Because relatively little is known about how SG fusion is regulated, we tested whether AdoMet could be acting via effects on the cytoskeleton and/or protein methylation. Previous studies have found that SG fusion is microtubule dependent (Ivanov et al., 2003), suggesting that AdoMet could act via effects of the microtubule cytoskeleton (Ivanov et al., 2003). However, AdoMet treatment did not cause an obvious defect in microtubule organization in HeLa cells (Fig. 7 E). Furthermore, the effects of AdoMet treatment on SG size and number were additive with those of the microtubule-depolymerizing drug, nocodazole (Fig. 7, E and F). This argues that AdoMet acts at a step that is distinct from the microtubule-dependent step of SG fusion.

One of the potential effects of AdoMet treatment is an increase in protein methylation. Given that SG formation and composition are known to be regulated by arginine methylation within RGG domains of SG components (Tsai et al., 2016), we next examined whether AdoMet could be acting via protein methylation. To test this possibility, we treated HeLa cells with AdoMet in the presence of the broad-spectrum methyltransferase inhibitor, adenosine dialdehyde (AdOx). Interestingly, AdoMet continued to robustly disrupt SG fusion in the presence of AdOx (Fig. 8). Thus, the effects of AdoMet on SG fusion in HeLa cells occur independently of the majority of methyltransferases.

AdoMet reduces SG formation in iPSC-derived MNs

Because both cell type and stress appeared to modulate the effects of AdoMet, we sought to test the effects of AdoMet on SG formation in cells where misregulation of SGs is linked to disease. Recent genetic studies have identified ALS-linked mutations in several RNA binding proteins (RBPs) that are either found in or regulate SGs, including TDP-43, FUS, and hnRNPA1/A2 (Kim et al., 2013; Kwiatkowski et al., 2009; Martinez et al., 2016; Sreedharan et al., 2008; Vance et al., 2009). ALS-associated mutations within these RBPs increase the conversion of phase-separated liquid droplets to form solid fibrillar structures in vitro (Lin et al., 2015; Molliex et al., 2015; Patel et al., 2015; Ryan et al., 2018) and increase SG assembly in cells (Kim et al., 2013). Neurons that contain these mutated RBPs and are continuously exposed to a lifetime of stress are thought to accumulate insoluble, pathological inclusions that contain many SG proteins. To test the effect of AdoMet on SG dynamics in ALS-associated MNs, we differentiated MNs using our previously established protocol (Martinez et al., 2016) from iPSC lines derived from patients with ALS-associated mutations in either TDP-43 (N352S) or FUS (R521G). The effects of AdoMet on arsenite- and puromycin-induced SGs were then examined and compared with control MNs from iPSC lines derived from a genetically related, but unaffected, family member and an unrelated healthy individual. AdoMet treatment reduced both the

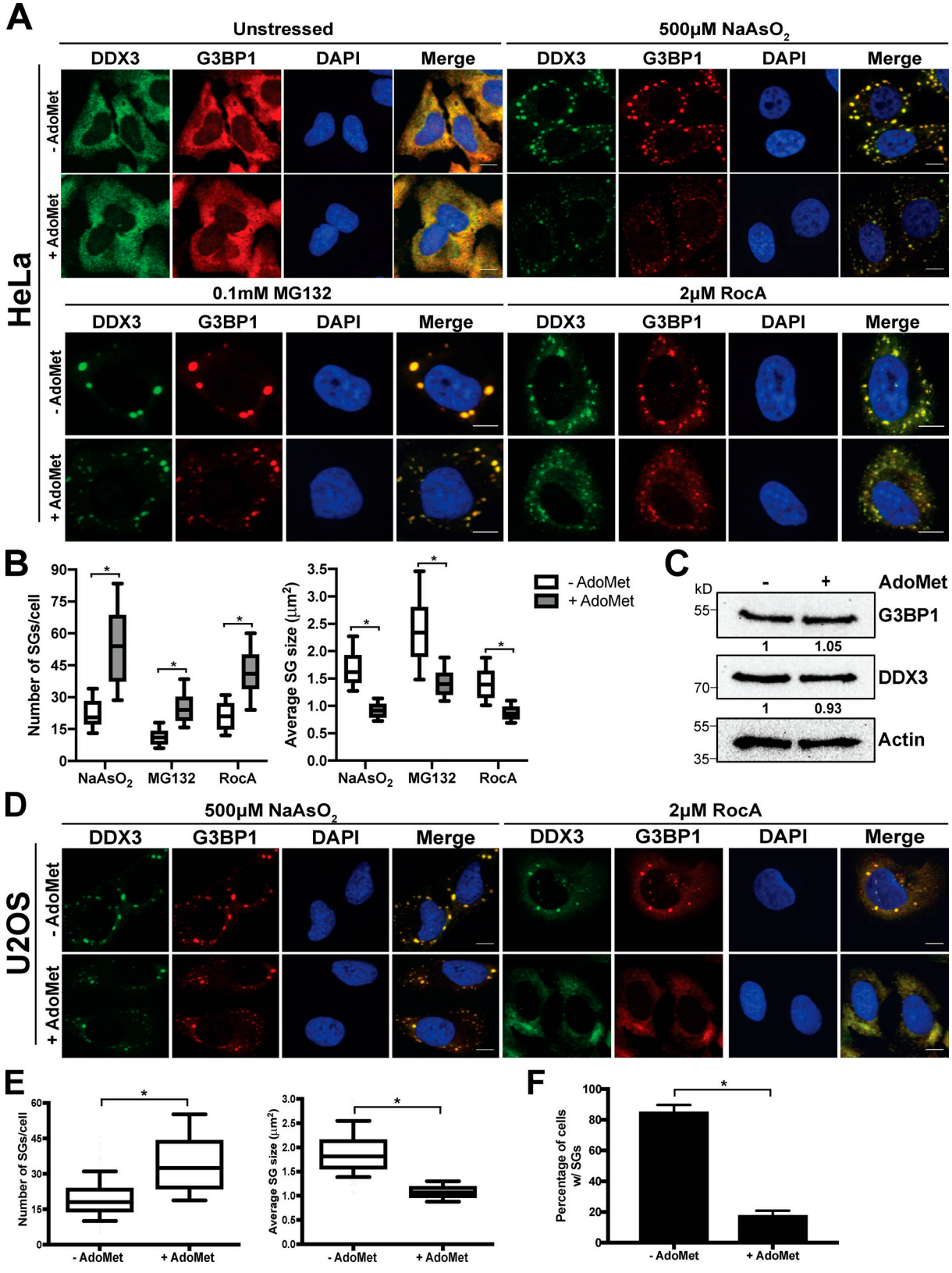

Figure 6. **AdoMet supplementation regulates SG assembly in HeLa and U2OS cells. (A)** Representative immunofluorescence images of AdoMet-treated or nontreated HeLa cells stressed with 500 µM $NaAsO_2$, 100 µM MG132, or 2 µM RocA and stained for DDX3 and G3BP1. **(B)** Box plot displaying the number of SGs/cell and average SG size from A. **(C)** Western blot analysis from HeLa cell lysates of AdoMet-treated and untreated cells. Values represent normalized protein levels of AdoMet-treated to untreated samples. Actin serves as a loading control. **(D)** Representative immunofluorescence images of AdoMet-treated or untreated U2OS cells stressed with 500 µM $NaAsO_2$ or 2 µM RocA and stained for DDX3 and G3BP1. **(E)** Box plot displaying the number of SGs/cell and average

SG size in response to arsenite stress from D. **(F)** Quantification of U2OS cells containing SGs in response to RocA treatment from D. Data are presented as average ± SEM of three independent replicates. Box plots in B and E are a compilation of three independent experiments. Scale bars in A and D are 10 µm. Statistical significance in B, E, and F was determined by one-tailed unpaired Student's *t* test, and in F, one-tailed paired Student's *t* test (*, $P < 0.05$). For box plots, the ends of the box mark the 25th and 75th percentiles. The median is marked by a horizontal line inside the box. The whiskers mark the minimum and maximum measurements.

number of SGs/cell as well as the total SG area/cell in both stresses (Fig. 9, A–D). Thus, AdoMet disrupts SG formation in MNs, and the effect is independent of the stress, unlike in HeLa and U2OS cells.

A hallmark of ALS includes the mislocalization of nuclear TDP-43 to cytoplasmic inclusions in spinal MNs of ALS patients (Bentmann et al., 2012; Blokhuis et al., 2013; Farg et al., 2013; Keller et al., 2012; Kim et al., 2013; Liu-Yesucevitz et al., 2010). MNs derived from ALS patients in both our study and previous studies exhibited prolonged cytoplasmic accumulation of TDP-43 following recovery from puromycin stress compared with MNs derived from healthy individuals (Fang et al., 2019). As a result, we next examined if AdoMet treatment affected TDP-43 recruitment to SGs in addition to decreasing the number of SGs that form. Interestingly, the SGs that formed in response to puromycin fail to recruit TDP-43 when the iPSC-derived MNs were pretreated with AdoMet. This effect was specific to TDP-43, as recruitment of Ataxin-2 to SGs was unaffected in AdoMet-pretreated iPSC-derived MNs (Fig. 9, E and F). Thus, in addition to decreasing SG formation, AdoMet treatment decreases the recruitment of TDP-43 to SGs that form in response to stress.

Discussion

SGs are believed to play a critical role in modulating gene expression programs in response to environmental and nutrient stresses. However, it has been unclear how changes in cellular activity regulate SG formation and composition. Our finding that Sam1 is recruited to yeast SGs in response to a specific nutrient stress and that the product of Sam1, AdoMet, regulates SG formation in both yeast and human cells suggests that the connections between metabolism and SG assembly might be broader than previously believed.

Stress-specific recruitment of metabolic enzymes to SGs

Recent work on the SG proteome suggests that SG composition can vary depending on the cell type and the nature of the stress (Markmiller et al., 2018). Because many of the stresses that trigger SG assembly are thought to alter metabolic activity, either directly or indirectly, one might expect metabolic enzymes to be a common component of SGs. However, few metabolic enzymes have been identified in proteomic and targeted studies of *Saccharomyces cerevisiae* SGs (Jain et al., 2016; Markmiller et al., 2018; Noree et al., 2019; Saad et al., 2017). Our identification of 17 metabolic enzymes that are recruited to SGs in response to physiological nutrient stresses, but are not recruited to SGs in response to multiple acute stresses, argues that SG composition is tailored to the nature of the stress and that chronic stresses might require reorganization of the metabolic network.

This result also helps to explain why no metabolic enzymes have been identified in previous proteomic studies of mammalian SGs. All of the stresses that are traditionally used to induce mammalian SGs, such as sodium azide, do not trigger the recruitment of metabolic enzymes to yeast SGs. Thus, one might expect to observe metabolic enzymes only in SGs that assemble in response to the mammalian equivalent of a stationary-phase nutrient stress.

Future studies directed at defining physiological nutrient stresses that induce SGs in mammalian cells would likely expand the connections between the SG proteome and metabolism.

Given that the recruitment of metabolic enzymes to SGs in yeast is stress specific, one might expect that additional targeting mechanisms were used for this class of proteins. Consistent with this, the metabolic enzymes recruited to SGs are not enriched in either IDR or LCS sequences relative to metabolic enzymes that are not targeted to SGs. Furthermore, the majority of the SG-associated metabolic enzymes do not possess a predicted RNA binding domain and have not been identified in high-throughput screens as RBPs. Thus, it is likely that the presence of neither IDR nor LCS sequences is sufficient to target these metabolic enzymes to SGs and that the recruitment mechanism is likely to involve additional stress-specific interaction domains.

Biphasic AdoMet regulation of yeast SG assembly

The stress-specific recruitment of metabolic enzymes suggested a novel route to identify metabolic pathways that might play a role in regulating SG assembly. Our focus on the product of Sam1, AdoMet, has uncovered unexpected parallels between how metabolites regulate metabolism and SG formation/composition. Metabolite regulation of metabolic pathway activity is biphasic. Critical metabolites can directly regulate enzyme activity over short time scales, but they also cause changes in the expression profile of a pathway when the metabolite is present or absent for long periods of time. Interestingly, we observed a similar two-phase regulation of SG formation and composition by AdoMet.

Brief treatments of log phase yeast with AdoMet were able to block SG formation in response to acute stresses without affecting expression levels of SG proteins. In contrast, genetic manipulations that caused sustained alterations in AdoMet levels affected the expression of the SG nucleator, Ded1. For instance, mutations in *SAM1* that decrease AdoMet production increase Ded1 protein levels. Because overexpression of Ded1 is known to trigger SG assembly (Hilliker et al., 2011), the increase in SG formation when AdoMet levels fall is likely due to its effect on Ded1 expression. Conversely, the deletion of *ADO1* in diauxic-phase cultures causes an increase in AdoMet levels and a reduction in both Ded1 protein levels and its localization to SGs.

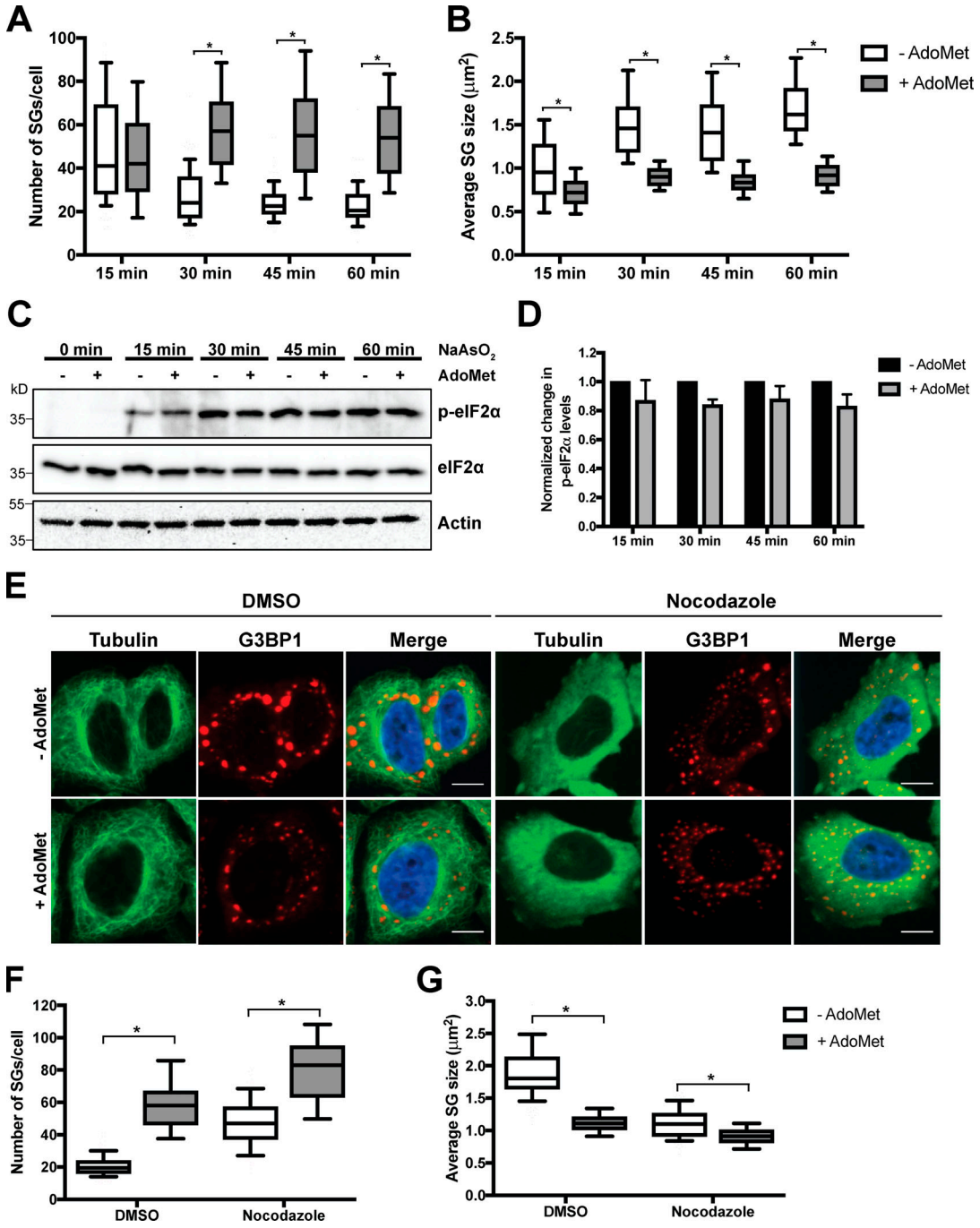

Figure 7. **SGs are unable to properly fuse in AdoMet-treated HeLa cells. (A)** Box plots depicting the number of SGs/cell in HeLa cells after the addition of 500 μM $NaAsO_2$. Gray boxes represent HeLa cells treated with AdoMet before stress. White boxes represent the untreated control. **(B)** Box plots depicting the average SG size at the indicated time points after addition of 500 μM $NaAsO_2$ for both AdoMet-treated (+AdoMet) and untreated (–AdoMet) HeLa cells. **(C)** Western blot analysis of HeLa cell lysates from the indicated time points after the addition of 500 μM $NaAsO_2$ from AdoMet-treated and untreated cells. Actin serves as a loading control. **(D)** Quantification of proteins levels from C. Data are presented as average ± SEM of three independent replicates. **(E)** Representative immunofluorescence images of HeLa cells stained for Tubulin and G3BP1 after treatment with 500 μM $NaAsO_2$-treated conditions. HeLa cells were treated with or without 4 mM AdoMet for 3 h and then DMSO or 5 μM nocodazole for 2 h before addition of $NaAsO_2$. Scale bar is 10 μM. **(F)** Box plot displaying the number of SGs/cell from E. **(G)** Box plot displaying quantification of the average SG size from E. Box plots in A, B, F, and G represent a compilation of three independent experiments. Statistical significance in A, B, F, and G was determined by one-tailed unpaired Student's *t* test (*, $P < 0.05$). For box plots, the ends of the box mark the 25th and 75th percentiles. The median is marked by a horizontal line inside the box. The whiskers mark the minimum and maximum measurements.

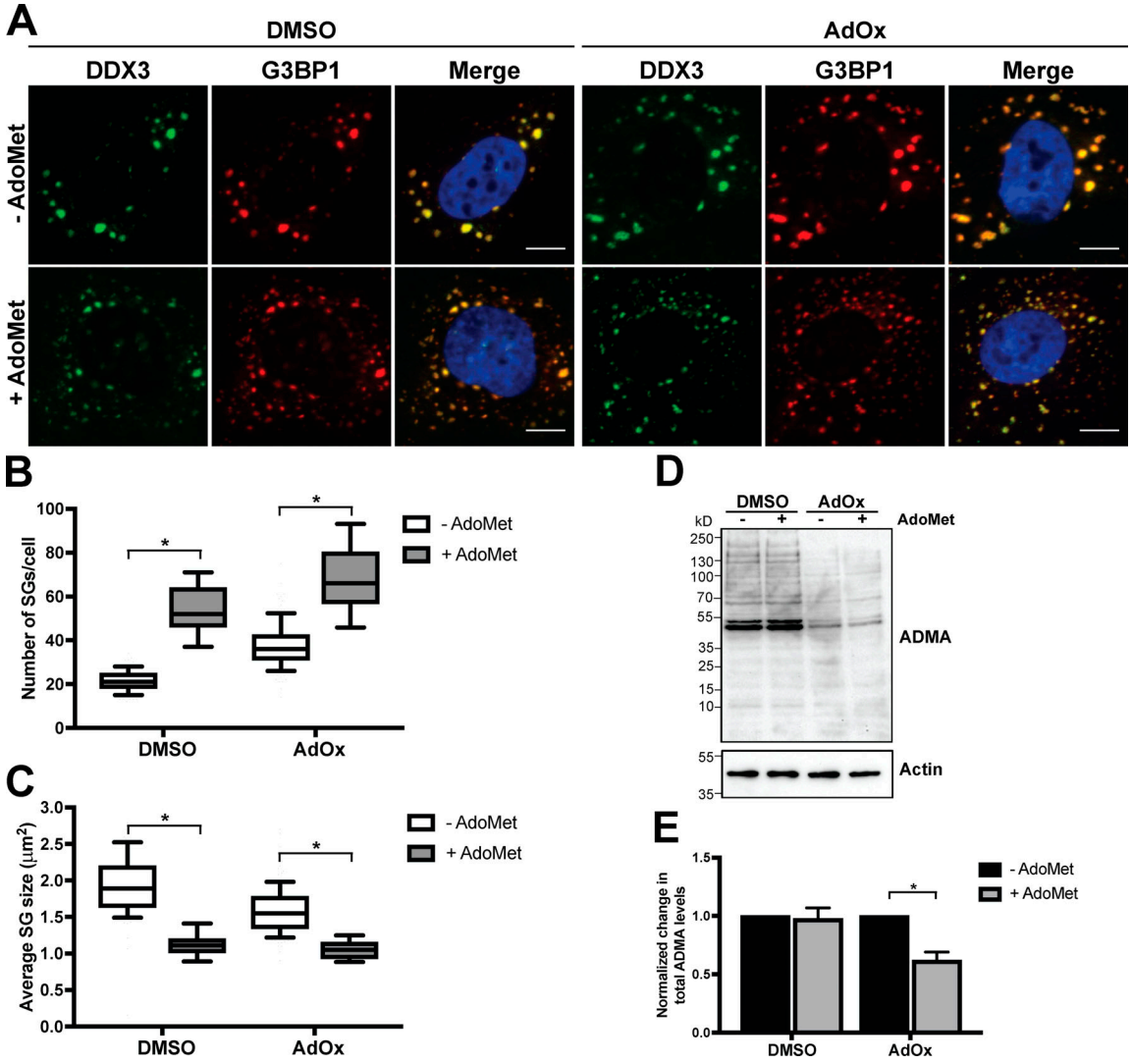

Figure 8. **AdoMet's effect on SG is not linked to protein methylation. (A)** Representative immunofluorescence images of HeLa cells stained for DDX3 and G3BP1 after 500 μM $NaAsO_2$ treatment. Before arsenite stress, HeLa cells were treated with DMSO or 20 μM AdOx for 48 h followed by the addition of 4 mM AdoMet for 3 h. Scale bar is 10 μM. **(B)** Box plot displaying the number of SGs/cell from A. **(C)** Box plot displaying quantification of the average SG size from A. **(D)** Western blot analysis from HeLa cell lysates that were treated with DMSO or 20 μM AdOx followed by addition of 4 mM AdoMet. Actin serves as a loading control. **(E)** Quantification of total ADMA levels from D. Data are presented as average ± SEM of three independent replicates. Box plots in B and C represent a compilation of three independent experiments. Statistical significance in B and C was determined by one-tailed unpaired Student's *t* test (*, $P < 0.05$). For box plots, the ends of the box mark the 25th and 75th percentiles. The median is marked by a horizontal line inside the box. The whiskers mark the minimum and maximum measurements.

Interestingly, this effect on Ded1 expression was posttranscriptional, since *ado1Δ* strains had elevated DED1 transcript levels even though the levels of Ded1 protein were decreased. Furthermore, aspects of this control loop might be conserved from yeast to humans, since protein levels of the human orthologue of Ded1, DDX3, have also been shown to be sensitive to AdoMet levels in Huh7 cells (Schröder et al., 2012).

These changes in SG composition in response to sustained elevation of AdoMet are not limited to Ded1. SGs in *ado1Δ* strain SGs also lacked other 5′ UTR mRNA-associated proteins, including eIF4G1 and eIF4E, while SG proteins associated with the 3′ UTR of mRNA (i.e., Pab1, Pbp1, and Pub1) were unaffected. Additionally, SGs in *ado1Δ* strains were defective in recruiting Sam1 and Ade17. With the exception of eIF4G1, none of these recruitment defects were due to a decrease in protein expression. Thus, sustained increases in AdoMet levels can selectively block recruitment of a subset of SG components in addition to down-regulating Ded1. Together, these results argue that AdoMet acts at short time scales to suppress SG formation, while chronic increases in AdoMet modify the SG proteome by affecting both the expression and recruitment of SG components. Interestingly, recent work has also identified acetyl-CoA as a candidate small-molecule regulator of SGs; however, its mechanism of action is unclear (Rollins et al., 2017). Future studies of how acetyl-CoA regulates SG assembly at short and long time scales will help determine whether biphasic regulation is a common feature of metabolite regulation of yeast SG formation.

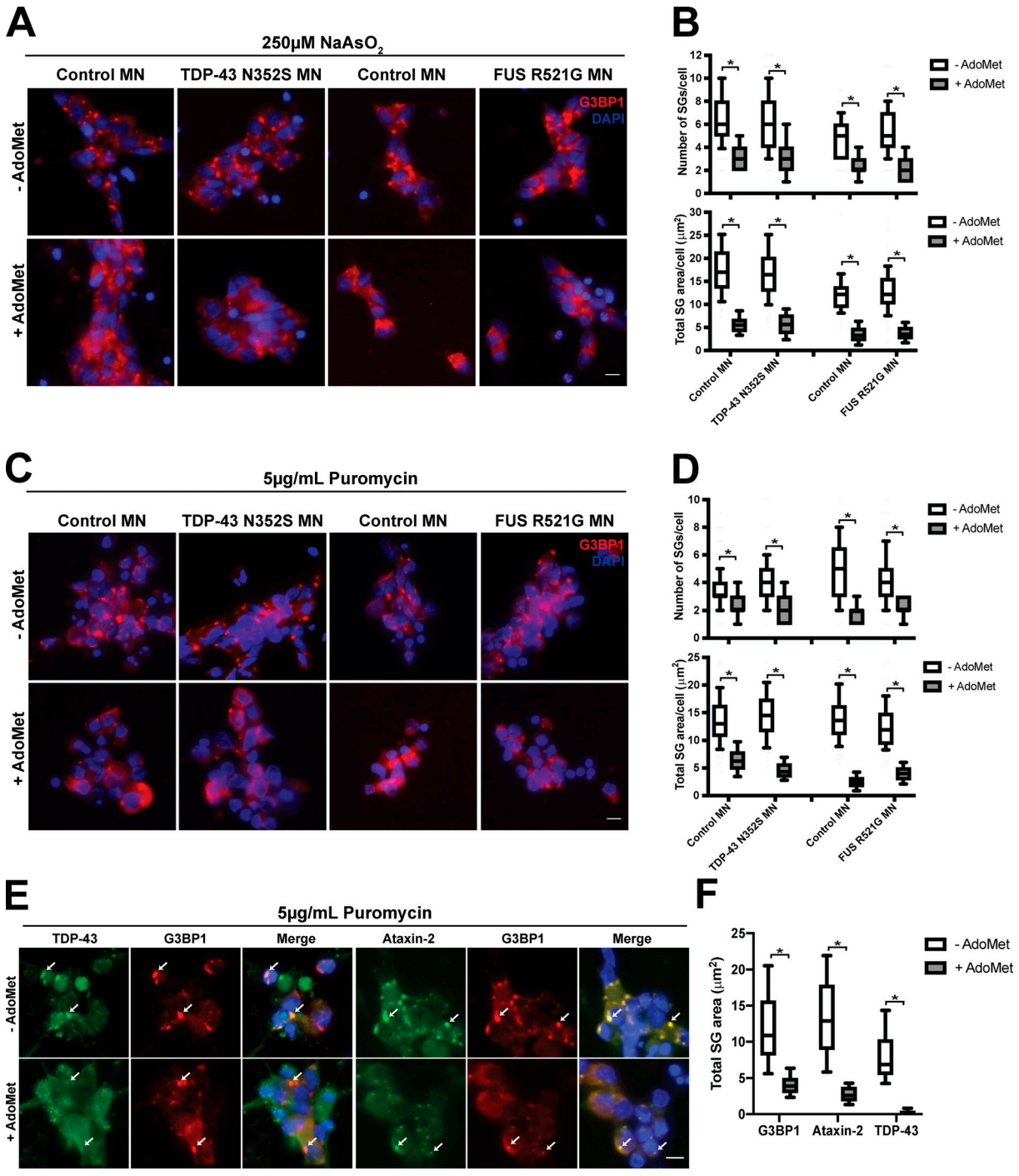

Figure 9. **AdoMet reduces SG formation in iPSC-derived MNs and reduces TDP-43 accumulation in SGs. (A)** Representative immunofluorescence images of AdoMet-treated or untreated control iPSC-derived MN lines and ALS-associated TDP-43 N352S and FUS R521G mutant iPSC-derived MN lines stained for TDP-43 and G3BP1 after treatment with 250 μM $NaAsO_2$. **(B)** Box plots displaying quantification of the number of SGs/cell and total SG area from A. **(C)** Representative immunofluorescence images of AdoMet-treated or untreated control iPSC-derived MN lines and ALS-associated TDP-43 N352S and FUS R521G mutant iPSC-derived MN lines stained for TDP-43 and G3BP1 after treatment with 5 μg/ml puromycin. **(D)** Box plots displaying quantification of the number of SGs/cell and total SG area from A. **(E)** Representative immunofluorescence images of AdoMet-treated or nontreated WT iPSC-derived MN lines stained for Ataxin 2, G3BP1, and TDP-43 after treatment with 5 μg/ml puromycin. **(F)** Box plots displaying quantification of the total SG area as measured by G3BP1, Ataxin-2, and TDP-43 from A. Box plots in B, D, and F represent a compilation of three independent experiments. Scale bars in A, C, and E are 10 μm. Statistical significance in B, D, and F was determined by one-tailed unpaired Student's *t* test (*, $P < 0.05$). For box plots, the ends of the box mark the 25th and 75th percentiles. The median is marked by a horizontal line inside the box. The whiskers mark the minimum and maximum measurements.

Although the molecular targets of AdoMet at either time scale are unclear, our initial characterization suggests that it does not act via protein methylation. Deletion of the Ded1 methyltransferase, HMT1, did not block the effect of elevated AdoMet levels. Similarly, treatment of mammalian cells with the broad-spectrum methyltransferase inhibitor, AdOx, did not block the effect of AdoMet on SGs. These experiments raise the possibility that AdoMet might disrupt SG formation by altering RNA methylation. Although mRNAs with m6A modifications are recruited into SGs (Anders et al., 2018; Wang et al., 2015), it remains to be determined whether the levels of mRNA methylation can alter the dynamics of SG formation.

Conservation of AdoMet-mediated SG regulation in mammalian cells

While yeast and mammalian SGs share a significant overlap in their proteome, not all aspects of composition and regulation are conserved. For instance, mammalian SGs mature by the fusion of small SGs into larger SGs, but fusion-based maturation has not been observed in yeast (Ivanov et al., 2003; Wheeler et al., 2016). Despite these differences, yeast and mammalian SGs are both regulated by AdoMet. Treatment of either yeast- or iPSC-derived MNs with AdoMet suppressed arsenite-induced SG formation in both cell types, arguing that AdoMet is a conserved small-molecule regulator of SGs.

Interestingly, although the acute effects of AdoMet on yeast and iPSC-derived MNs are comparable, AdoMet treatment had distinct effects on SG formation in cancer-derived cell lines. Treatment of HeLa cells with AdoMet before oxidative, proteotoxic, and translational stress resulted in SGs that were greater in number and smaller in size. This suggests that AdoMet treatment disrupts SG fusion in cancer-derived cell lines rather than blocking SG formation. Furthermore, this effect is microtubule independent, implying that AdoMet treatment is disrupting a novel step in the SG fusion process. One possible reason that AdoMet treatment disrupts different steps in SG formation in HeLa cells compared with iPSC-derived MNs is that cancer cell lines and nondividing primary cells have distinct metabolic profiles. Future studies examining how basal cell metabolism alters AdoMet's effects on SG formation will likely provide new insights into what makes particular cells sensitive or resistant to stress.

Most provocatively, AdoMet treatment suppressed SG formation in iPSC-derived MNs that expressed mutated forms of TDP-43 and FUS found in ALS patients. AdoMet was effective in blocking SG assembly in these disease models, even though these mutated forms of TDP-43 and FUS have an increased propensity to phase separate (Ling et al., 2013; Mackenzie et al., 2017; Murakami et al., 2015; Patel et al., 2015). Thus, aberrant, pathogenic SGs are just as sensitive to AdoMet treatment as normal SGs. This argues that AdoMet acts at a step in SG formation that is common to both the conventional SG assembly pathway and the pathways used by aggregation-prone variants of TDP-43 and FUS. Furthermore, the few SGs that form in mutant MNs pretreated with AdoMet fail to recruit TDP-43. AdoMet exhibits a planar aromatic moiety similar to other known active molecules that are known to reduce SG assembly and block other ALS-associated RBPs (Fang et al., 2019). Thus, the ability of AdoMet to suppress the formation of pathological SGs argues that pathways that control either AdoMet levels or the SG response to AdoMet, presenting an exciting and tractable therapeutic approach for ALS and other neurodegenerative diseases.

Materials and methods

Yeast strains and growth

All yeast experiments were performed in *S. cerevisiae* budding yeast in the BY4741 background. All yeast strains were grown at 30°C unless otherwise indicated in either YPD medium (1% yeast extract, 2% peptone, and 2% dextrose) or synthetic defined (SD) medium (0.17% yeast nitrogen base without ammonium sulfate or amino acids, 0.5% ammonium sulfate, amino acids, and 2% glucose).

A complete list of strains used in this study is given in Table S4. All yeast strains were derived from a parent strain with the genotype MATa his3Δ1 leu2Δ0 met15Δ0 ura3Δ0 (BY4741). Generation of endogenous GFP-tagged strains and gene disruption was performed using standard PCR-mediated techniques (Wach et al., 1994). A complete list of oligonucleotides used in this study is given in Table S5. Strains from the GFP collection (Howson et al., 2005) were used as background strains for the production of dual fluorescent–tagged strains used in RNA granule screen. For all other experiments, newly made strains were generated using BY4741 (Dharmacon) as the parental strain.

To generate Ded1 and Sam1 mutants, the full-length coding sequence was amplified from the genomic locus and subcloned into the pFA6a-GFP-KanMx6 plasmid upstream of the GFP sequence. With the resulting plasmids as templates, site-directed mutagenesis was used to generate point mutations. Ded1-GFP and Sam1-GFP variants were introduced into their respective endogenous loci by PCR-amplifying cassettes that contained the coding sequence of Ded1-GFP or Sam1-GFP, a kanamycin resistance marker, and a 50-bp sequence homologous to downstream of their respective stop codons. These cassettes were introduced into yeast using standard yeast transformation protocols. Genomic DNA was extracted from resulting transformants, and the loci were PCR amplified and sequenced to verify the presence of the correct mutation.

Preparation of samples for yeast microscopy

For acquiring images from RNA granule screen, cells were grown in YPD at 30°C for 1 and 5 d and fixed before imaging. Briefly, 0.1 ml 37% formaldehyde was added to 1 ml of culture and rotated for 15 min at RT. Fixed cells were then spun down and washed with water before resuspending in 1 M sorbitol. Cells were stored for up to 1 wk at 4°C or imaged immediately. For the remaining experiments, live-cell imaging was used. Cells were grown in indicated medium at 30°C to either log phase or 1-d time point and spun down. Samples were concentrated in their existing medium, and cells were imaged immediately.

Heat shock, sodium azide, glucose deprivation, and ethanol shock were performed as described previously with methionine deprivation under similar conditions. Briefly, cells were grown

in indicated medium (YPD or SD) overnight at 30°C and then back-diluted into fresh medium to an OD_{600} of 0.2 and grown at 30°C to log phase. For heat shock experiments, cells were transferred to a water bath set at 46°C or remained at 30°C for 10 min. For NaN_3 experiments, yeast cultures were treated with 0.5% NaN_3 or water for 30 min at 30°C before imaging. For glucose-deprivation experiments, cells were collected and washed in 30°C prewarmed medium lacking glucose (YP or SD Glu−) followed by resuspension again in 30°C prewarmed medium lacking glucose. Cells were then placed back at 30°C for 30 min and then imaged immediately. For ethanol shock, yeast cultures were collected and washed in 30°C prewarmed SD medium with ethanol (SD EtOH 6%) as its sole carbon source followed by resuspension again in 30°C prewarmed SD medium with ethanol. Cells were placed back at 30°C for 30 min and imaged immediately. For methionine-deprivation experiments, cells were collected and washed with 30°C prewarmed SD medium lacking methionine followed by resuspension again in 30°C prewarmed SD medium lacking methionine. Cells were placed back at 30°C for 30 min and imaged immediately. For AdoMet-supplemented experiments, yeast cultures were grown overnight in YPD medium at 30°C and then back-diluted into YPD with 250 µM AdoMet (Sigma-Aldrich). Cells were then grown to the desired time point.

RNA isolation and quantitative PCR (qPCR)

Total RNA was obtained by harvesting 40 OD_{600} units of cells from the 1-d time point and resuspending pellets in RNA lysis buffer (10 mM EDTA and 50 mM NaOAc, pH 5.5). Next, SDS was added to a final volume of 1%. Samples were then subjected to a series of hot acid phenol/chloroform, acid phenol/chloroform, and chloroform extractions followed by precipitation. 5 µg of RNA was used to create cDNA using the SuperScript III First-Strand Synthesis System (Invitrogen) following the manufacturer's protocol. qPCR was performed using SYBR Green PCR Master Mix (Applied Biosystems). The relative levels of transcripts were calculated using the ΔΔCt method and normalized to *ACT1*.

Yeast metabolomics

Metabolite extraction was performed as indicated in Boer et al. (2010). Briefly, 20 ml of −20°C 100% liquid chromatography–mass spectrometry (LC-MS)–grade methanol was added to 10 ml of yeast cultures that were grown to either log phase or 24 h (1-d time point). Next, samples were spun down at 4,000 rpm for 5 min at −10°C. The supernatant was decanted, and the pellet was resuspended in −20°C LC-MS–grade extraction buffer (40:40:20 acetonitrile/methanol/water) and then incubated at 4°C for 15 min. Resuspensions were pelleted again, and the supernatant was saved. Extraction buffer was added again to the pellets and incubated for 15 min. Cells were pelleted again, and the supernatant was added to the previous fraction and stored at −80°C.

Quantitative analysis of SAM, AdoMet, and methionine by LC-MS was performed using conditions previously described (Vliet et al., 2019). Briefly, analysis was performed on a TQ-XS triple-quadrupole mass spectrometer (Waters) coupled to an I-class ultraperformance LC system (Waters). Separations were performed on a ZIC-pHILIC column (2.1 × 150 mm, 5 µM; EMD Millipore). The mobile phases were water with 15 mM ammonium bicarbonate adjusted to pH 9.6 with ammonium hydroxide (A) and acetonitrile (B). The flow rate was 200 µl/min and the column was held at 50°C. The injection volume was 1 µl. The gradient was as follows: 0 min, 90% B; 1.5 min, 90% B; 16 min, 20% B; 18 min, 20% B; 20 min, 90% B; and 28 min, 90% B.

The MS was operated in selected reaction monitoring mode. Source and desolvation temperatures were 150°C and 500°C, respectively. Desolvation gas was set to 1,000 liter/h and cone gas to 150 liter/h. Collision gas flow was 0.15 ml/min. All gases were nitrogen except the collision gas, which was argon. Capillary voltage was 1 kV in positive ion mode. A quality control sample, generated by pooling equal aliquots of each sample, was analyzed every three to six injections to monitor system stability and performance. Samples were analyzed in random order. Data were processed using Skyline software (MacLean et al., 2010).

Polysome profile analysis

200 ml of WT cells (BY4741) were grown to log phase (OD_{600} ~0.5) in YPD medium with or without 250 µM AdoMet (Sigma-Aldrich) at 30°C. Once cells reached log phase, the 200-ml culture was split into two flasks containing 100 ml each, and one was treated with 0.05% sodium azide or switched into medium lacking glucose (YP) for 30 min at 30°C. Before harvesting, cells were treated with 100 µg/ml cyclohexamide (Sigma-Aldrich) and allowed to shake for an additional 2 min at 30°C. Cultures were then spun down for 5 min at 4,000 rpm at 4°C, and the pellet was washed and resuspended in 1.5 ml ice-cold polysome lysis buffer (20 mM Tris-HCl, pH 8.0, 140 mM KCl, 1.5 mM $MgCl_2$, 100 µg/ml cyclohexamide, and 1% Triton X-100). An equal volume of acid-washed glass beads was added to the resuspensions, and lysis was performed by vortexing samples for 30 s a total of eight times with 1 min of recovery on ice in between cycles. Lysates were then cleared by centrifuging samples for 5 min at 2,000 rpm at 4°C. The supernatant was recovered and then spun for 10 min at 14,000 rpm at 4°C. The supernatant was collected, and OD_{260} values were determined using a NanoDrop Spectrophotometer. 50 OD_{260} units were then loaded onto a 10–50% linear sucrose gradient and centrifuged for 3 h at 35,000 rpm at 4°C. Gradients were collected from the top using a Biocomp Nano Fractionator, which continuously measured A254 values to generate polysome traces.

Mammalian cell culture growth conditions

The HeLa-S3 cell line is derived from human female cervical adenocarcinoma tissue, and the U2OS cell line is derived from human female osteosarcoma tissue. Both HeLa and U2OS cell lines were maintained in DMEM (Gibco), 10% FBS (Corning), and 1% penicillin/streptomycin (Gibco) at 37°C and 5% CO_2 in a humidified incubator.

Adult human primary fibroblasts carrying TARDBP (N352S) mutation and from a control individual were obtained by Dr. John Ravits (University of California, San Diego). Primary fibroblasts were cultured in DMEM supplemented with 10% FBS, nonessential amino acids, and L-glutamine at 37°C and 5% CO_2 in

a humidified incubator. To generate iPSCs, fibroblasts were transduced with Cytotune iPS Sendai Reprogramming Kit, according to the manufacturer's protocol (Invitrogen). The human iPSC line carrying ALS-associated FUS (R521G) mutation was previously reprogrammed from primary fibroblasts obtained by Franca Cambia, Edward Kasarskis, and Haining Zhu (University of Kentucky, Lexington, KY), as described (Kapeli et al., 2016). All iPSCs were maintained on Matrigel-coated plates (BD Biosciences) in mTeSR1 growth medium (Stem Cell Technologies) at 37°C and 5% CO_2 in a humidified incubator. Colonies were expanded by clump-passaging using enzyme-free dissociation buffer (EDTA). Informed consent was obtained from all individuals before sample collection. The use of patient fibroblasts for research was approved by the University of California, San Diego Institutional Review Board.

Generation of iPSC-derived MNs

Human MNs were differentiated from iPSCs as previously described (Markmiller et al., 2018). Briefly, immediately before differentiation, iPSCs were passaged with Accutase (StemCell Technologies) and grown as a monolayer on feeder-free plates in mTeSR1. Once the cells reached >90% confluence, medium was changed daily with N2B27 medium (DMEM/F12 + GlutaMAX [Life Technologies], 1% N-2 supplement, 2% B-27 supplement [Thermo Fisher Scientific], 200 µM ascorbic acid [Sigma-Aldrich], and 1% penicillin/streptomycin) and supplemented with 1 µM dorsomorphin dihydrochloride, 10 µM SB431542, and 4 µM CHIR99021 (Tocris) for 6 d. From day 7 to 18, cells were fed daily with N2B27 medium supplemented with 1 µM dorsomorphin dihydrochloride, 10 µM SB431542, 200 nM smoothened agonist (SAG; Tocris), and 1.5 µM retinoic acid (RA; Sigma-Aldrich). On day 18, cells were dissociated using Accutase and transferred to plates coated first with 0.001% wt/vol poly-D-lysine hydrobromide and poly-L-ornithine (Sigma-Aldrich) overnight, followed by an overnight incubation of 20 µg/ml laminin (Life Technologies) at 37°C, 5% CO_2. The dissociated cells were seeded in N2B27 medium supplemented with 2 ng/ml recombinant human brain-derived neurotrophic factor, 2 ng/ml recombinant human glial cell line–derived neurotrophic factor, 2 ng/ml recombinant human ciliary neurotrophic factor (PeproTech), 1.5 µM RA, 200 nM SAG, and 10 µM Y-26732 ROCK inhibitor (Tocris). On day 20, medium was modified by reducing ROCK inhibitor to 2 µM. On day 22, RA and SAG was withdrawn, and 2 µM *N*-[*N*-(3,5-difluorophenacetyl-L-alanyl)]-*S*-phenylglycine t-butyl ester (DAPT; Tocris) was added to the medium. For imaging, cells were replated sparsely onto poly-D-lysine hydrobromide/poly-L-ornithine/laminin-coated 8-well glass chamber slides (Millipore) in the same medium on day 24. At 26 d, DAPT was withdrawn from the medium.

Mammalian cell immunofluorescence

HeLa and U2OS cells were passaged and plated onto glass coverslips in 12-well plates and grown for 24 h. For AdoMet treatment, 4 mM AdoMet was added to wells for 3 h before the application of stress or nocodazole (Sigma-Aldrich). For AdOx experiments, cells were grown in the presence of 20 µM before addition of AdoMet. To induce SG formation, sodium arsenite (Sigma-Aldrich) was added to a final concentration of 500 µM and incubated for 1 h. For MG132 (Sigma-Aldrich) and RocA (Sigma-Aldrich) experiments, cells were incubated with compounds for 2 h in a final concentration of 100 µM and 2 µM, respectively. Cells were then washed with PBS and fixed in 4% PFA (Sigma-Aldrich) for 20 min. After removal of fixative, cells were washed with PBS and then permeabilized in 0.5% Triton X-100/PBS for 15 min. After permeabilization, cells were washed with PBS and then incubated with blocking solution (4% BSA/PBS) for 30 min. Primary antibodies (1:100 mouse anti-DDX3, Santa Cruz Biotech, sc-365768; and 1:1,000 rabbit anti-G3BP1, Sigma-Aldrich, G6046) were diluted in blocking solution and added to cells overnight at 4°C. After PBS washes, secondary antibodies (1:200 donkey anti-rabbit 568, Invitrogen, A10042; and 1:200 goat anti-mouse 488, Invitrogen, A-11029) were incubated for 2 h in the dark. Cells were washed with PBS, and DAPI was added before mounting coverslips with Vectashield (Vector Laboratories).

On day 28 of culture, iPSC-derived MNs were pretreated with 4 mM AdoMet for 3 h before the addition of 250 µM sodium arsenite for 1 h or 5 µg/ml puromycin for 24 h. After stress, cells were fixed with 4% PFA for 45 min at RT. After three washes with PBS, the cells were simultaneously blocked and permeabilized with 5% goat serum, 0.1% Triton X-100, and 1× PBS for 1 h at RT. Cells were rinsed with once with PBS and incubated with primary antibody (1:500 mouse anti-TARBP, Abnova, H00023435-M01; and 1:1,000 rabbit anti-G3BP1, Sigma-Aldrich, G6046) diluted in 0.01% Triton X-100, 5% goat serum, and 1× PBS overnight at 4°C. After five washes with 0.01% Triton X-100 and 1× PBS, secondary antibody (1:1,000 goat anti-mouse Alexa Fluor 488, Invitrogen, A-11029; and goat anti-rabbit Alexa Fluor 555, Invitrogen, A-21428) diluted in 0.01% Triton X-100, 5% goat serum, and 1× PBS was added for 1 h at RT. Cells were washed 10 times in 0.01% Triton X-100 and 1× PBS before nuclei stain with DAPI (1:5,000 vol/vol in PBS) for 15 min at RT. After one wash with 1× PBS, cells were preserved in 50% vol/vol glycerol in PBS.

Western blot analysis

For yeast samples, whole-cell extracts were prepared via NaOH extraction as indicated in Kushnirov (2000). Cells were grown in YPD medium at 30°C to either log phase or 1-d time point. Next, 1 OD_{600} (log phase) or 2.5 OD_{600} (1 d) was spun down and resuspended in 0.1 N NaOH. After incubation at RT for 5 min, cells were spun down and then resuspended in 2× sample buffer with protease inhibitors (Sigma-Aldrich). Samples were boiled for 5 min at 95°C and incubated on ice for 3 min before centrifugation once more. Supernatants were stored at −20°C or used immediately.

For HeLa cells, lysates were obtained by first rinsing cells with cold 1× PBS to remove debris and medium. Next, radioimmunoprecipitation assay buffer (50 mM Tris-HCl, pH 7.5, 150 mM NaCl, 1% Triton X-100, 1% sodium deoxycholate, 0.1% SDS, and 2 mM EDTA) with protease inhibitors was added, and cells were scraped and centrifuged for 10 min at 15,000 rpm at 4°C. Protein concentration was then determined by Bradford assay (Bio-Rad Protein Assay Dye Reagent Concentrate) and

normalized across samples. Next, 4× sample buffer was added, and samples were boiled for 5 min at 95°C and placed on ice for 3 min before centrifugation. Samples were stored at −20°C or used immediately.

Samples were resolved on 10% SDS-PAGE gels and subsequently transferred to nitrocellulose membrane using semidry conditions. Membranes were then incubated in blocking solution (5% milk in TBST 0.1%) for 1 h. After TBST 0.1% washes, membranes were incubated in primary antibody overnight at 4°C: 1:5,000 rabbit anti-GFP (Torrey Pines Biolabs, TP401), 1:2,500 mouse anti-mCherry (Novus Biologicals, NBP1-96752), 1:10,000 mouse anti-PGK1 (Invitrogen, 459250), 1:500 mouse anti-DDX3 (Santa Cruz Biotech, sc-365768), 1:10,000 rabbit anti-G3BP (Sigma-Aldrich, G6046), 1:500 mouse anti-ACTA (Developmental Studies Hybridoma Bank, JLA20), 1:1,000 rabbit anti-eIF2α (Cell Signaling Technology, 9722S), 1:1,000 rabbit anti-phospho-eIF2α Ser51 (Cell Signaling Technology, 3398S), and 1:1,000 rabbit-ADMA (Cell Signaling Technology, 13522S). Primary antibody was removed and washed with TBST 0.1% before adding HRP-conjugated secondary antibody (1:10,000 donkey anti-rabbit, Invitrogen, A16023; and 1:2,500 sheep anti-mouse, Abcam, ab6808) in 5% blocking solution for 2 h at RT. Membranes were then washed with TBST 0.1% and then incubated in Thermo Fisher Scientific Pierce ECL Western Blotting Substrate. Chemiluminescence was detected using FluorChem E system (Protein Simple). Quantification of protein levels was performed using densitometry methods by comparing signals to internal control signal (PGK1 for yeast samples or actin for HeLa cells).

Microscopy and image analysis

All images (with the exception of MN experiments) were acquired on a Zeiss Axiovert 200M fluorescent microscope equipped with a CSU-X1 spinning disk (Yokogawa), a Chrome-MLE laser source (Toptica Photonics), and μManager v1.4 software at RT. For acquisition of yeast, a 2-μm Z-stack was taken with slices at 0.25-μm intervals using a Nikon 40× 0.65-NA oil (or 100× 1.25-NA oil for intensity ratio determination) objective. Mammalian cell images were acquired by taking slices at 0.3-μm intervals to obtain a 3-μm Z-stack using the 40× 0.65-NA oil objective. Images for MNs were acquired on a Nikon Ti2 microscope equipped with a Nikon Qi2 Camera, Lumencor SpectraX LED light engine, Semrock quad bandpass filter cube with barrier filters, and NIS Elements v5.11 software. Images were taken using a Nikon 40× 0.95-NA objective at RT. For acquisition, five random nonoverlapping positions within each well of a 96-well plate were generated. At each position, an autofocusing routine was run to identify the Z-plane with the highest contrast in the 405-nm channel, and a symmetrical 7-μm-thick Z-stack centered around this focal plane with 0.9-μm steps was captured.

For all images, optimal Z-projections were obtained using Fiji along with subsequent image analysis. Colocalization quantification was determined manually as the percentage of the number of GFP foci overlapped with mCherry foci divided by the total number of GFP foci. To determine intensity ratio analysis, maximum intensities of foci were measured along with the average intensity of the cytoplasm of that cell. Each value was background-corrected by subtracting the average intensity of the image with no cell. Intensity ratios were calculated by dividing the corrected foci intensity by the corrected cytoplasm intensity.

For mammalian cell image analysis, single cells were isolated using the freehand selection tool in Fiji. The number and size of foci as well as total SG area were then determined using the Fiji 3D Objects Counter plugin. Data were exported to Microsoft Excel and pooled for further analysis.

Quantification and statistical analysis

One-tailed paired Student's *t* test was used when comparing the averages between two samples. For dot plot and box plot analysis, Welch's *t* test for unequal size and variance and one-tailed unpaired Student's *t* test were used to determine the significance, respectively. Data distribution was assumed to be normal, although this was not formally tested. Statistical analysis was performed using GraphPad Prism 7 software.

Online supplemental material

Fig. S1 summarizes the effects of the *SAM1* D121N mutation on Sam1 and Sam2 recruitment to SGs. Fig. S2 highlights the effects of AdoMet manipulation on the metabolites in the methionine biosynthetic pathway. Fig. S3 compares the effects of high AdoMet levels on the foci formation of P-bodies and metabolic enzymes found to associate with SGs. Fig. S4 illustrates that AdoMet-mediated suppression is stress specific and time dependent in yeast. Fig. S5 compares the time-dependent effects of AdoMet on arsenite-induced SGs in mammalian cells. Table S1 lists the results of the metabolic enzyme-RNA granule screen. Table S2 shows the domain analysis of metabolic enzymes identified in the RNA granule screen. Table S3 displays the domain analysis of metabolic enzymes with low to no colocalization with RNA granules. Table S4 lists the strains used in this study. Table S5 displays the oligonucleotides used in this study.

Acknowledgments

We thank the Nikon Imaging Center, University of California, San Diego, for imaging assistance. We also thank the members of the Bennett Lab (University of California, San Diego) for assistance with the polysome analysis experiments. LC-MS analysis was performed at the Metabolomics Core Facility at University of California, Riverside (metabolomics.iigb.ucr.edu).

Work from the Wilhelm laboratory was supported by a grant to J.E. Wilhelm from the Collaborative Innovation Awards program of Howard Hughes Medical Institute and the James Wilhelm Memorial Fund. K. Begovich is a Howard Hughes Medical Institute Gilliam Fellow. Work from the Yeo laboratory was supported by grants to G. Yeo from the National Institutes of Health (HG004659), Target ALS (20193440), and the ALS Association (272 and 438).

G. Yeo is co-founder, member of the Board of Directors, on the SAB, equity holder, and paid consultant for Locana and Eclipse BioInnovations. G. Yeo is a visiting professor at the National University of Singapore. G. Yeo's interests have been reviewed and approved by the University of California, San

Diego, in accordance with its conflict of interest policies. The remaining authors declare no competing financial interests.

Author contributions: K. Begovich performed the yeast SG screen, carried out all the experiments, and analyzed all the data. A.Q. Vu was essential for culturing the iPSC-derived MNs. K. Begovich, A.Q. Vu, G. Yeo, and J.E. Wilhelm designed the study and wrote the manuscript.

Submitted: 25 April 2019
Revised: 21 February 2020
Accepted: 20 April 2020

References

Aguilera-Gomez, A., M. Zacharogianni, M.M. van Oorschot, H. Genau, R. Grond, T. Veenendaal, K.S. Sinsimer, E.R. Gavis, C. Behrends, and C. Rabouille. 2017. Phospho-Rasputin stabilization by Sec16 is required for stress granule formation upon amino acid starvation. *Cell Rep.* 20: 935–948. https://doi.org/10.1016/j.celrep.2017.06.042

Anders, M., I. Chelysheva, I. Goebel, T. Trenkner, J. Zhou, Y. Mao, S. Verzini, S.B. Qian, and Z. Ignatova. 2018. Dynamic m^{6}A methylation facilitates mRNA triaging to stress granules. *Life Sci. Alliance.* 1. e201800113. https://doi.org/10.26508/lsa.201800113

Arimoto, K., H. Fukuda, S. Imajoh-Ohmi, H. Saito, and M. Takekawa. 2008. Formation of stress granules inhibits apoptosis by suppressing stress-responsive MAPK pathways. *Nat. Cell Biol.* 10:1324–1332. https://doi.org/10.1038/ncb1791

Aulas, A., M.M. Fay, S.M. Lyons, C.A. Achorn, N. Kedersha, P. Anderson, and P. Ivanov. 2017. Stress-specific differences in assembly and composition of stress granules and related foci. *J. Cell Sci.* 130:927–937. https://doi.org/10.1242/jcs.199240

Banani, S.F., H.O. Lee, A.A. Hyman, and M.K. Rosen. 2017. Biomolecular condensates: organizers of cellular biochemistry. *Nat. Rev. Mol. Cell Biol.* 18:285–298. https://doi.org/10.1038/nrm.2017.7

Bentmann, E., M. Neumann, S. Tahirovic, R. Rodde, D. Dormann, and C. Haass. 2012. Requirements for stress granule recruitment of fused in sarcoma (FUS) and TAR DNA-binding protein of 43 kDa (TDP-43). *J. Biol. Chem.* 287:23079–23094. https://doi.org/10.1074/jbc.M111.328757

Blokhuis, A.M., E.J. Groen, M. Koppers, L.H. van den Berg, and R.J. Pasterkamp. 2013. Protein aggregation in amyotrophic lateral sclerosis. *Acta Neuropathol.* 125:777–794. https://doi.org/10.1007/s00401-013-1125-6

Boer, V.M., C.A. Crutchfield, P.H. Bradley, D. Botstein, and J.D. Rabinowitz. 2010. Growth-limiting intracellular metabolites in yeast growing under diverse nutrient limitations. *Mol. Biol. Cell.* 21:198–211. https://doi.org/10.1091/mbc.e09-07-0597

Chen-Plotkin, A.S., V.M. Lee, and J.Q. Trojanowski. 2010. TAR DNA-binding protein 43 in neurodegenerative disease. *Nat. Rev. Neurol.* 6:211–220. https://doi.org/10.1038/nrneurol.2010.18

Decker, C.J., D. Teixeira, and R. Parker. 2007. Edc3p and a glutamine/asparagine-rich domain of Lsm4p function in processing body assembly in Saccharomyces cerevisiae. *J. Cell Biol.* 179:437–449. https://doi.org/10.1083/jcb.200704147

Eisinger-Mathason, T.S., J. Andrade, A.L. Groehler, D.E. Clark, T.L. Muratore-Schroeder, L. Pasic, J.A. Smith, J. Shabanowitz, D.F. Hunt, I.G. Macara, et al. 2008. Codependent functions of RSK2 and the apoptosis-promoting factor TIA-1 in stress granule assembly and cell survival. *Mol. Cell.* 31:722–736. https://doi.org/10.1016/j.molcel.2008.06.025

Erce, M.A., D. Abeygunawardena, J.K. Low, G. Hart-Smith, and M.R. Wilkins. 2013. Interactions affected by arginine methylation in the yeast protein-protein interaction network. *Mol. Cell. Proteomics.* 12:3184–3198. https://doi.org/10.1074/mcp.M113.031500

Fang, M.Y., S. Markmiller, A.Q. Vu, A. Javaherian, W.E. Dowdle, P. Jolivet, P.J. Bushway, N.A. Castello, A. Baral, M.Y. Chan, et al. 2019. Small-molecule modulation of TDP-43 recruitment to stress granules prevents persistent TDP-43 accumulation in ALS/FTD. *Neuron.* 103:802–819.e11. https://doi.org/10.1016/j.neuron.2019.05.048

Farg, M.A., K.Y. Soo, S.T. Warraich, V. Sundaramoorthy, I.P. Blair, and J.D. Atkin. 2013. Ataxin-2 interacts with FUS and intermediate-length polyglutamine expansions enhance FUS-related pathology in amyotrophic lateral sclerosis. *Hum. Mol. Genet.* 22:717–728. https://doi.org/10.1093/hmg/dds479

Gilks, N., N. Kedersha, M. Ayodele, L. Shen, G. Stoecklin, L.M. Dember, and P. Anderson. 2004. Stress granule assembly is mediated by prion-like aggregation of TIA-1. *Mol. Biol. Cell.* 15:5383–5398. https://doi.org/10.1091/mbc.e04-08-0715

Grignaschi, E., G. Cereghetti, F. Grigolato, M.R.G. Kopp, S. Caimi, L. Faltova, S. Saad, M. Peter, and P. Arosio. 2018. A hydrophobic low-complexity region regulates aggregation of the yeast pyruvate kinase Cdc19 into amyloid-like aggregates *in vitro*. *J. Biol. Chem.* 293:11424–11432. https://doi.org/10.1074/jbc.RA117.001628

Harding, H.P., I. Novoa, Y. Zhang, H. Zeng, R. Wek, M. Schapira, and D. Ron. 2000. Regulated translation initiation controls stress-induced gene expression in mammalian cells. *Mol. Cell.* 6:1099–1108. https://doi.org/10.1016/S1097-2765(00)00108-8

Hilliker, A., Z. Gao, E. Jankowsky, and R. Parker. 2011. The DEAD-box protein Ded1 modulates translation by the formation and resolution of an eIF4F-mRNA complex. *Mol. Cell.* 43:962–972. https://doi.org/10.1016/j.molcel.2011.08.008

Hofweber, M., S. Hutten, B. Bourgeois, E. Spreitzer, A. Niedner-Boblenz, M. Schifferer, M.D. Ruepp, M. Simons, D. Niessing, T. Madl, et al. 2018. Phase Separation of FUS Is Suppressed by Its Nuclear Import Receptor and Arginine Methylation. *Cell.* 173:706–719.e13. https://doi.org/10.1016/j.cell.2018.03.004

Howson, R., W.K. Huh, S. Ghaemmaghami, J.V. Falvo, K. Bower, A. Belle, N. Dephoure, D.D. Wykoff, J.S. Weissman, and E.K. O'Shea. 2005. Construction, verification and experimental use of two epitope-tagged collections of budding yeast strains. *Comp. Funct. Genomics.* 6:2–16. https://doi.org/10.1002/cfg.449

Ivanov, P.A., E.M. Chudinova, and E.S. Nadezhdina. 2003. Disruption of microtubules inhibits cytoplasmic ribonucleoprotein stress granule formation. *Exp. Cell Res.* 290:227–233. https://doi.org/10.1016/S0014-4827(03)00290-8

Jain, S., J.R. Wheeler, R.W. Walters, A. Agrawal, A. Barsic, and R. Parker. 2016. ATPase-Modulated Stress Granules Contain a Diverse Proteome and Substructure. *Cell.* 164:487–498. https://doi.org/10.1016/j.cell.2015.12.038

Kanai, M., M. Masuda, Y. Takaoka, H. Ikeda, K. Masaki, T. Fujii, and H. Iefuji. 2013. Adenosine kinase-deficient mutant of Saccharomyces cerevisiae accumulates S-adenosylmethionine because of an enhanced methionine biosynthesis pathway. *Appl. Microbiol. Biotechnol.* 97:1183–1190. https://doi.org/10.1007/s00253-012-4261-3

Kapeli, K., G.A. Pratt, A.Q. Vu, K.R. Hutt, F.J. Martinez, B. Sundararaman, R. Batra, P. Freese, N.J. Lambert, S.C. Huelga, et al. 2016. Distinct and shared functions of ALS-associated proteins TDP-43, FUS and TAF15 revealed by multisystem analyses. *Nat. Commun.* 7:12143. https://doi.org/10.1038/ncomms12143

Kato, M., T.W. Han, S. Xie, K. Shi, X. Du, L.C. Wu, H. Mirzaei, E.J. Goldsmith, J. Longgood, J. Pei, et al. 2012. Cell-free formation of RNA granules: low complexity sequence domains form dynamic fibers within hydrogels. *Cell.* 149:753–767. https://doi.org/10.1016/j.cell.2012.04.017

Kedersha, N., S. Chen, N. Gilks, W. Li, I.J. Miller, J. Stahl, and P. Anderson. 2002. Evidence that ternary complex (eIF2-GTP-tRNA(i)(Met))-deficient preinitiation complexes are core constituents of mammalian stress granules. *Mol. Biol. Cell.* 13:195–210. https://doi.org/10.1091/mbc.01-05-0221

Kedersha, N., P. Ivanov, and P. Anderson. 2013. Stress granules and cell signaling: more than just a passing phase? *Trends Biochem. Sci.* 38: 494–506. https://doi.org/10.1016/j.tibs.2013.07.004

Keller, B.A., K. Volkening, C.A. Droppelmann, L.C. Ang, R. Rademakers, and M.J. Strong. 2012. Co-aggregation of RNA binding proteins in ALS spinal motor neurons: evidence of a common pathogenic mechanism. *Acta Neuropathol.* 124:733–747. https://doi.org/10.1007/s00401-012-1035-z

Khong, A., T. Matheny, S. Jain, S.F. Mitchell, J.R. Wheeler, and R. Parker. 2017. The stress granule transcriptome reveals principles of mRNA accumulation in stress granules. *Mol. Cell.* 68:808–820.e5. https://doi.org/10.1016/j.molcel.2017.10.015

Kim, B., H.J. Cooke, and K. Rhee. 2012. DAZL is essential for stress granule formation implicated in germ cell survival upon heat stress. *Development.* 139:568–578. https://doi.org/10.1242/dev.075846

Kim, H.J., N.C. Kim, Y.D. Wang, E.A. Scarborough, J. Moore, Z. Diaz, K.S. MacLea, B. Freibaum, S. Li, A. Molliex, et al. 2013. Mutations in prion-like domains in hnRNPA2B1 and hnRNPA1 cause multisystem proteinopathy and ALS. *Nature.* 495:467–473. https://doi.org/10.1038/nature11922

Kushnirov, V.V.. 2000. Rapid and reliable protein extraction from yeast. *Yeast.* 16:857–860. https://doi.org/10.1002/1097-0061(20000630)16:9<857::AID-YEA561>3.0.CO;2-B

Kwiatkowski, T.J., Jr., D.A. Bosco, A.L. Leclerc, E. Tamrazian, C.R. Vanderburg, C. Russ, A. Davis, J. Gilchrist, E.J. Kasarskis, T. Munsat, et al. 2009. Mutations in the FUS/TLS gene on chromosome 16 cause familial amyotrophic lateral sclerosis. *Science*. 323:1205–1208. https://doi.org/10.1126/science.1166066

Kwon, S., Y. Zhang, and P. Matthias. 2007. The deacetylase HDAC6 is a novel critical component of stress granules involved in the stress response. *Genes Dev*. 21:3381–3394. https://doi.org/10.1101/gad.461107

Lin, Y., D.S.W. Protter, M.K. Rosen, and R. Parker. 2015. Formation and Maturation of Phase-Separated Liquid Droplets by RNA-Binding Proteins. *Molecular Cell*. 60:208–219. https://doi.org/10.1016/j.molcel.2015.08.018

Ling, S.C., M. Polymenidou, and D.W. Cleveland. 2013. Converging mechanisms in ALS and FTD: disrupted RNA and protein homeostasis. *Neuron*. 79:416–438. https://doi.org/10.1016/j.neuron.2013.07.033

Liu-Yesucevitz, L., A. Bilgutay, Y.J. Zhang, T. Vanderweyde, A. Citro, T. Mehta, N. Zaarur, A. McKee, R. Bowser, M. Sherman, et al. 2010. Tar DNA binding protein-43 (TDP-43) associates with stress granules: analysis of cultured cells and pathological brain tissue. *PLoS One*. 5. e13250. https://doi.org/10.1371/journal.pone.0013250

Low, J.K., G. Hart-Smith, M.A. Erce, and M.R. Wilkins. 2013. Analysis of the proteome of Saccharomyces cerevisiae for methylarginine. *J. Proteome Res*. 12:3884–3899. https://doi.org/10.1021/pr400556c

Mackenzie, I.R., A.M. Nicholson, M. Sarkar, J. Messing, M.D. Purice, C. Pottier, K. Annu, M. Baker, R.B. Perkerson, A. Kurti, et al. 2017. TIA1 mutations in amyotrophic lateral sclerosis and frontotemporal dementia promote phase separation and alter stress granule dynamics. *Neuron*. 95:808–816.e9. https://doi.org/10.1016/j.neuron.2017.07.025

MacLean, B., D.M. Tomazela, N. Shulman, M. Chambers, G.L. Finney, B. Frewen, R. Kern, D.L. Tabb, D.C. Liebler, and M.J. MacCoss. 2010. Skyline: an open source document editor for creating and analyzing targeted proteomics experiments. *Bioinformatics*. 26:966–968. https://doi.org/10.1093/bioinformatics/btq054

Markmiller, S., S. Soltanieh, K.L. Server, R. Mak, W. Jin, M.Y. Fang, E.C. Luo, F. Krach, D. Yang, A. Sen, et al. 2018. Context-Dependent and Disease-Specific Diversity in Protein Interactions within Stress Granules. *Cell*. 172:590–604.e13. https://doi.org/10.1016/j.cell.2017.12.032

Martinez, F.J., G.A. Pratt, E.L. Van Nostrand, R. Batra, S.C. Huelga, K. Kapeli, P. Freese, S.J. Chun, K. Ling, C. Gelboin-Burkhart, et al. 2016. Protein-RNA Networks Regulated by Normal and ALS-Associated Mutant HNRNPA2B1 in the Nervous System. *Neuron*. 92:780–795. https://doi.org/10.1016/j.neuron.2016.09.050

Matia-González, A.M., E.E. Laing, and A.P. Gerber. 2015. Conserved mRNA-binding proteomes in eukaryotic organisms. *Nat. Struct. Mol. Biol*. 22:1027–1033. https://doi.org/10.1038/nsmb.3128

Mazroui, R., S. Di Marco, R.J. Kaufman, and I.-E. Gallouzi. 2007. Inhibition of the ubiquitin-proteasome system induces stress granule formation. *Mol. Biol. Cell*. 18:2603–2618. https://doi.org/10.1091/mbc.e06-12-1079

Mitchell, S.F., S. Jain, M. She, and R. Parker. 2013. Global analysis of yeast mRNPs. *Nat. Struct. Mol. Biol*. 20:127–133. https://doi.org/10.1038/nsmb.2468

Molliex, A., J. Temirov, J. Lee, M. Coughlin, A.P. Kanagaraj, H.J. Kim, T. Mittag, and J.P. Taylor. 2015. Phase Separation by Low Complexity Domains Promotes Stress Granule Assembly and Drives Pathological Fibrillization. *Cell*. 163:123–133. https://doi.org/10.1016/j.cell.2015.09.015

Murakami, T., S. Qamar, J.Q. Lin, G.S. Schierle, E. Rees, A. Miyashita, A.R. Costa, R.B. Dodd, F.T. Chan, C.H. Michel, et al. 2015. ALS/FTD Mutation-Induced Phase Transition of FUS Liquid Droplets and Reversible Hydrogels into Irreversible Hydrogels Impairs RNP Granule Function. *Neuron*. 88:678–690. https://doi.org/10.1016/j.neuron.2015.10.030

Narayanaswamy, R., M. Levy, M. Tsechansky, G.M. Stovall, J.D. O'Connell, J. Mirrielees, A.D. Ellington, and E.M. Marcotte. 2009. Widespread reorganization of metabolic enzymes into reversible assemblies upon nutrient starvation. *Proc. Natl. Acad. Sci. USA*. 106:10147–10152. https://doi.org/10.1073/pnas.0812771106

Noree, C., K. Begovich, D. Samilo, R. Broyer, E. Monfort, and J.E. Wilhelm. 2019. A quantitative screen for metabolic enzyme structures reveals patterns of assembly across the yeast metabolic network. *Mol. Biol. Cell*. 30:2721–2736. https://doi.org/10.1091/mbc.E19-04-0224

Noree, C., B.K. Sato, R.M. Broyer, and J.E. Wilhelm. 2010. Identification of novel filament-forming proteins in Saccharomyces cerevisiae and Drosophila melanogaster. *J. Cell Biol*. 190:541–551. https://doi.org/10.1083/jcb.201003001

Orrù, S., P. Coni, A. Floris, R. Littera, C. Carcassi, V. Sogos, and C. Brancia. 2016. Reduced stress granule formation and cell death in fibroblasts with the A382T mutation of TARDBP gene: evidence for loss of TDP-43 nuclear function. *Hum. Mol. Genet*. 25:4473–4483. https://doi.org/10.1093/hmg/ddw276

Panas, M.D., P. Ivanov, and P. Anderson. 2016. Mechanistic insights into mammalian stress granule dynamics. *J. Cell Biol*. 215:313–323. https://doi.org/10.1083/jcb.201609081

Patel, A., H.O. Lee, L. Jawerth, S. Maharana, M. Jahnel, M.Y. Hein, S. Stoynov, J. Mahamid, S. Saha, T.M. Franzmann, et al. 2015. A Liquid-to-Solid Phase Transition of the ALS Protein FUS Accelerated by Disease Mutation. *Cell*. 162:1066–1077. https://doi.org/10.1016/j.cell.2015.07.047

Protter, D.S.W., and R. Parker. 2016. Principles and Properties of Stress Granules. *Trends Cell Biol*. 26:668–679. https://doi.org/10.1016/j.tcb.2016.05.004

Protter, D.S.W., B.S. Rao, B. Van Treeck, Y. Lin, L. Mizoue, M.K. Rosen, and R. Parker. 2018. Intrinsically Disordered Regions Can Contribute Promiscuous Interactions to RNP Granule Assembly. *Cell Rep*. 22:1401–1412. https://doi.org/10.1016/j.celrep.2018.01.036

Reineke, L.C., S.A. Cheema, J. Dubrulle, and J.R. Neilson. 2018. Chronic starvation induces noncanonical pro-death stress granules. *J. Cell Sci*. 131. jcs220244. https://doi.org/10.1242/jcs.220244

Rollins, M., S. Huard, A. Morettin, J. Takuski, T.T. Pham, M.D. Fullerton, J. Côté, and K. Baetz. 2017. Lysine acetyltransferase NuA4 and acetyl-CoA regulate glucose-deprived stress granule formation in Saccharomyces cerevisiae. *PLoS Genet*. 13. e1006626. https://doi.org/10.1371/journal.pgen.1006626

Ryan, V.H., G.L. Dignon, G.H. Zerze, C.V. Chabata, R. Silva, A.E. Conicella, J. Amaya, K.A. Burke, J. Mittal, and N.L. Fawzi. 2018. Mechanistic View of hnRNPA2 Low-Complexity Domain Structure, Interactions, and Phase Separation Altered by Mutation and Arginine Methylation. *Mol. Cell*. 69:465–479.e7. https://doi.org/10.1016/j.molcel.2017.12.022

Saad, S., G. Cereghetti, Y. Feng, P. Picotti, M. Peter, and R. Dechant. 2017. Reversible protein aggregation is a protective mechanism to ensure cell cycle restart after stress. *Nat. Cell Biol*. 19:1202–1213. https://doi.org/10.1038/ncb3600

Scherrer, T., N. Mittal, S.C. Janga, and A.P. Gerber. 2010. A screen for RNA-binding proteins in yeast indicates dual functions for many enzymes. *PLoS One*. 5. e15499. https://doi.org/10.1371/journal.pone.0015499

Schröder, P.C., J. Fernández-Irigoyen, E. Bigaud, A. Serna, R. Renández-Alcoceba, S.C. Lu, J.M. Mato, J. Prieto, and F.J. Corrales. 2012. Proteomic analysis of human hepatoma cells expressing methionine adenosyltransferase I/III: Characterization of DDX3X as a target of S-adenosylmethionine. *J. Proteomics*. 75:2855–2868. https://doi.org/10.1016/j.jprot.2012.01.009

Shang, Y., and E.J. Huang. 2016. Mechanisms of FUS mutations in familial amyotrophic lateral sclerosis. *Brain Res*. 1647:65–78. https://doi.org/10.1016/j.brainres.2016.03.036

Shen, H., H. Wang, Q. Liu, H. Liu, M. Teng, and X. Li. 2014. Structural insights into RNA recognition properties of glyceraldehyde-3-phosphate dehydrogenase 3 from Saccharomyces cerevisiae. *IUBMB Life*. 66:631–638. https://doi.org/10.1002/iub.1313

Sreedharan, J., I.P. Blair, V.B. Tripathi, X. Hu, C. Vance, B. Rogelj, S. Ackerley, J.C. Durnall, K.L. Williams, E. Buratti, et al. 2008. TDP-43 mutations in familial and sporadic amyotrophic lateral sclerosis. *Science*. 319:1668–1672. https://doi.org/10.1126/science.1154584

Swisher, K.D., and R. Parker. 2010. Localization to, and effects of Pbp1, Pbp4, Lsm12, Dhh1, and Pab1 on stress granules in Saccharomyces cerevisiae. *PLoS One*. 5. e10006. https://doi.org/10.1371/journal.pone.0010006

Taylor, J.C., and G.D. Markham. 1999. The bifunctional active site of s-adenosylmethionine synthetase. Roles of the active site aspartates. *J. Biol. Chem*. 274:32909–32914. https://doi.org/10.1074/jbc.274.46.32909

Taylor, J.C., and G.D. Markham. 2000. The bifunctional active site of S-adenosylmethionine synthetase. Roles of the basic residues. *J. Biol. Chem*. 275:4060–4065. https://doi.org/10.1074/jbc.275.6.4060

Tsai, W.C., S. Gayatri, L.C. Reineke, G. Sbardella, M.T. Bedford, and R.E. Lloyd. 2016. Arginine Demethylation of G3BP1 Promotes Stress Granule Assembly. *J. Biol. Chem*. 291:22671–22685. https://doi.org/10.1074/jbc.M116.739573

Tsai, W.C., L.C. Reineke, A. Jain, S.Y. Jung, and R.E. Lloyd. 2017. Histone arginine demethylase JMJD6 is linked to stress granule assembly through demethylation of the stress granule-nucleating protein G3BP1. *J. Biol. Chem*. 292:18886–18896. https://doi.org/10.1074/jbc.M117.800706

Van Treeck, B., D.S.W. Protter, T. Matheny, A. Khong, C.D. Link, and R. Parker. 2018. RNA self-assembly contributes to stress granule formation and defining the stress granule transcriptome. *Proc. Natl. Acad. Sci. USA*. 115:2734–2739. https://doi.org/10.1073/pnas.1800038115

Vance, C., B. Rogelj, T. Hortobágyi, K.J. De Vos, A.L. Nishimura, J. Sreedharan, X. Hu, B. Smith, D. Ruddy, P. Wright, et al. 2009. Mutations in FUS, an RNA processing protein, cause familial amyotrophic lateral sclerosis type 6. *Science*. 323:1208–1211. https://doi.org/10.1126/science.1165942

Vliet, S.M.F., S. Dasgupta, N.R.L. Sparks, J.S. Kirkwood, A. Vollaro, M. Hur, N.I. Zur Nieden, and D.C. Volz. 2019. Maternal-to-zygotic transition as a potential target for niclosamide during early embryogenesis. *Toxicol. Appl. Pharmacol*. 380. 114699. https://doi.org/10.1016/j.taap.2019.114699

Wach, A., A. Brachat, R. Pöhlmann, and P. Philippsen. 1994. New heterologous modules for classical or PCR-based gene disruptions in Saccharomyces cerevisiae. *Yeast*. 10:1793–1808. https://doi.org/10.1002/yea.320101310

Wang, X., B.S. Zhao, I.A. Roundtree, Z. Lu, D. Han, H. Ma, X. Weng, K. Chen, H. Shi, and C. He. 2015. N(6)-methyladenosine Modulates Messenger RNA Translation Efficiency. *Cell*. 161:1388–1399. https://doi.org/10.1016/j.cell.2015.05.014

Wheeler, J.R., T. Matheny, S. Jain, R. Abrisch, and R. Parker. 2016. Distinct stages in stress granule assembly and disassembly. *eLife*. 5. e18413. https://doi.org/10.7554/eLife.18413

Wippich, F., B. Bodenmiller, M.G. Trajkovska, S. Wanka, R. Aebersold, and L. Pelkmans. 2013. Dual specificity kinase DYRK3 couples stress granule condensation/dissolution to mTORC1 signaling. *Cell*. 152:791–805. https://doi.org/10.1016/j.cell.2013.01.033

Yang, X., Y. Shen, E. Garre, X. Hao, D. Krumlinde, M. Cvijović, C. Arens, T. Nyström, B. Liu, and P. Sunnerhagen. 2014. Stress granule-defective mutants deregulate stress responsive transcripts. *PLoS Genet*. 10. e1004763. https://doi.org/10.1371/journal.pgen.1004763

JCB

Supplemental material

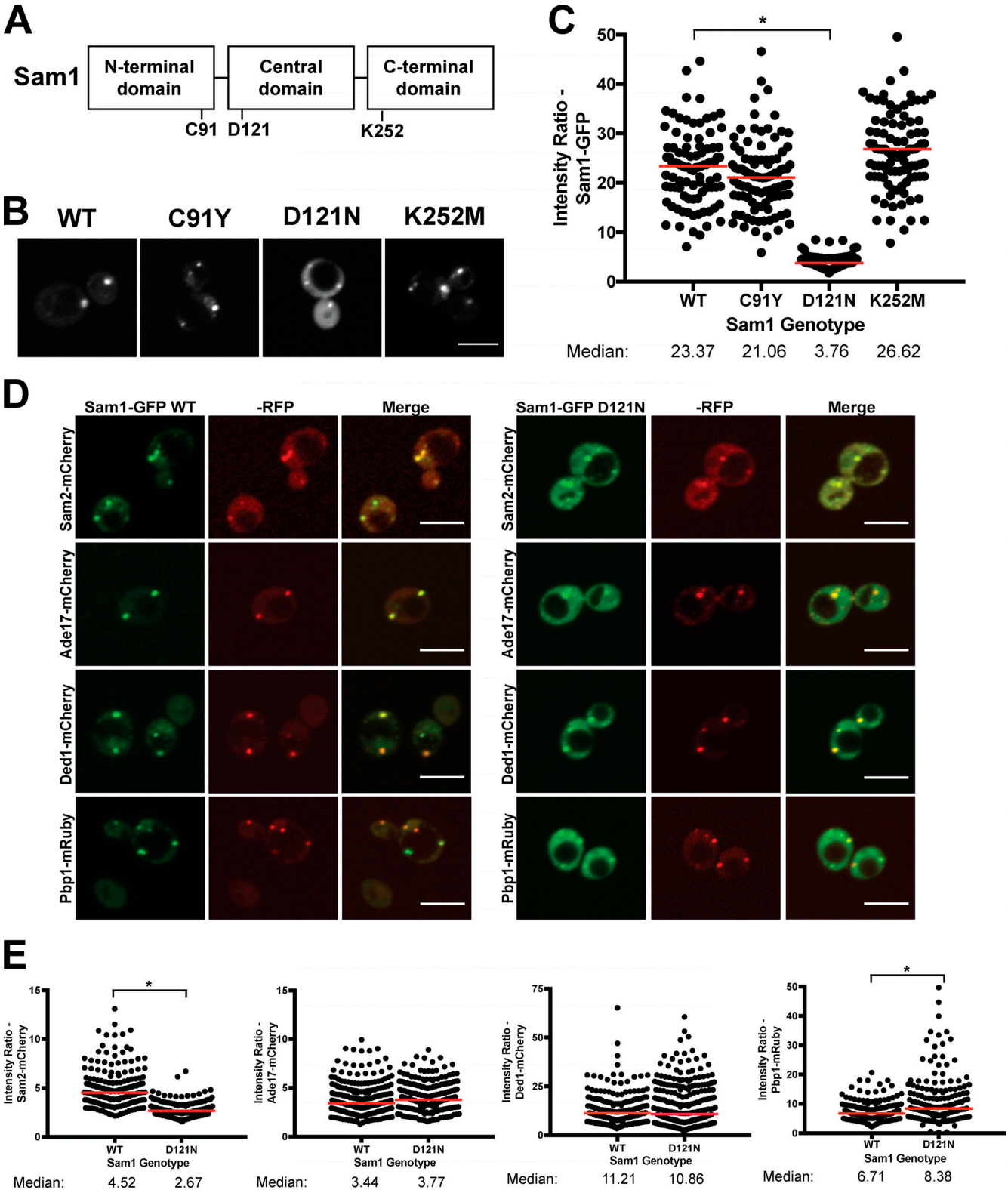

Figure S1. **Mutation in the ATP binding domain of Sam1 inhibits recruitment of Sam1 and Sam2 to SGs. (A)** Domain organization of Sam1 protein noting the location of inactivating point mutations. **(B)** Representative fluorescence images of endogenously expressed WT or mutant Sam1-GFP. **(C)** Dot plot displaying foci-to-cytoplasm ratios for endogenously expressed WT and mutant alleles of Sam1-GFP. Red lines mark median value. **(D)** Representative fluorescence images of colocalization endogenously expressed WT or D121N Sam1-GFP with RFP-tagged Sam2, Ade17, Ded1, or Pbp1. **(E)** Dot plot displaying foci-to-cytoplasm ratios for endogenously expressed RFP-tagged Sam2, Ade17, Ded1, and Pbp1 in both WT and *SAM1 D121N* backgrounds. Red lines mark median value. Scale bars in B and D are 5 µM. Statistical significance in C and E was determined by one-tailed Welch's *t* test (*, $P < 0.05$).

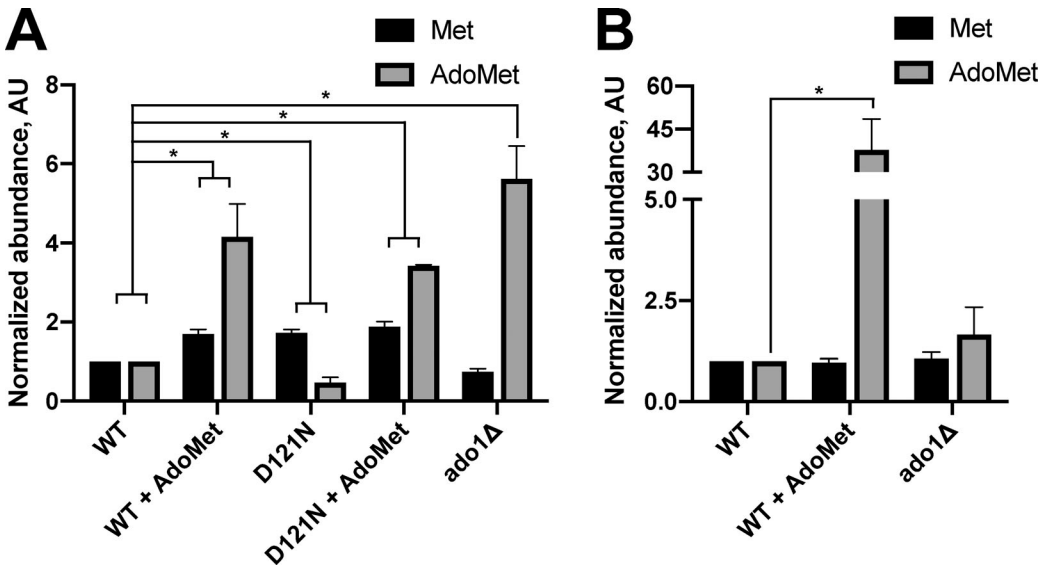

Figure S2. **Genetic disruptions of *SAM1* and *ADO1* result in changes in methionine biosynthetic pathway intermediates. (A)** Quantification of methionine and AdoMet from WT, 250 µM-treated WT, *SAM1* D121N, 250 µM-treated *SAM1* D121N, and *ado1Δ* strains at 1-d time point. Values are normalized to WT samples. **(B)** Quantification of methionine and AdoMet from WT, 250 µM-treated WT, and *ado1Δ* strains at log phase. Bar graphs are presented as average ± SEM of three independent replicates. Values are normalized to WT samples. Statistical significance was determined by one-tailed paired Student's *t* test (*, $P < 0.05$).

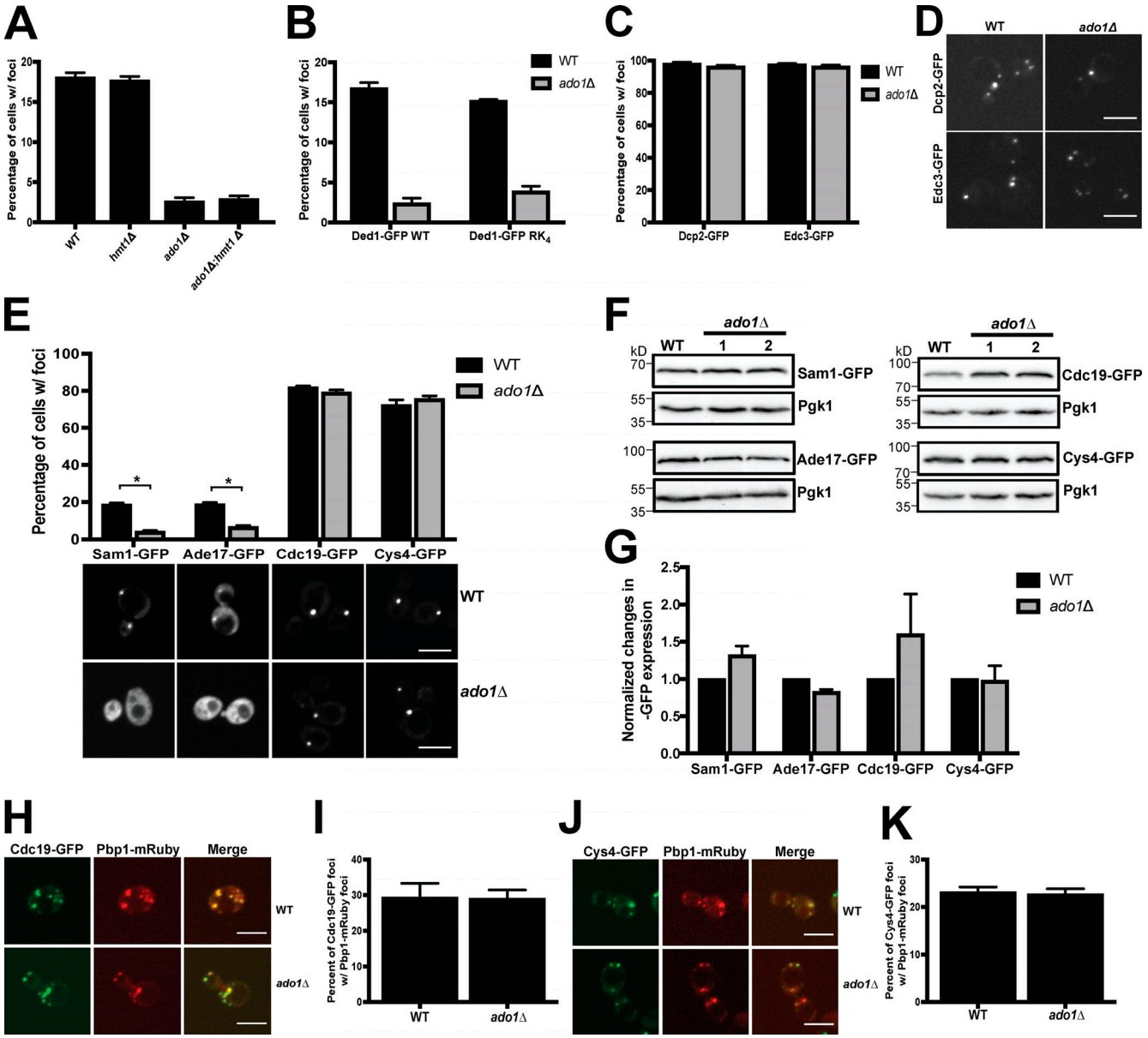

Figure S3. **Characterization of the SG phenotype in *ado1Δ* strains. (A)** Quantification of cells with Ded1-GFP foci in WT, *hmt1Δ*, *ado1Δ*, and *ado1Δ;hmt1Δ* background strains at 1-d time point. **(B)** Quantification of cells with foci in WT and *ado1Δ* backgrounds expressing either WT or RK 4 Ded1-GFP. **(C)** Quantification of cells with foci for P-body markers (Dcp2 and Edc3) in WT and *ado1Δ* background strains at 1-d time point. **(D)** Representative images from D. **(E)** Quantification and representative fluorescent images of WT and ado1Δ strains with GFP-tagged metabolic enzymes at 1-d time point. *, P < 0.05. **(F)** Western blot analysis of strains used in E at 1-d time point. **(G)** Quantification of proteins levels from F. Pgk1 serves as a loading control. **(H)** Representative fluorescent images of WT or *ado1Δ* strains expressing Cdc19-GFP and Pbp1-mRuby at 1-d time point. **(I)** Quantification of the degree of colocalization of Cdc19-GFP foci to Pbp1-mRuby foci in WT and ado1Δ strains. **(J)** Representative fluorescent images of WT or *ado1Δ* strains expressing Cys4-GFP and Pbp1-mRuby at 1-d time point. **(K)** Quantification of the degree of colocalization of Cys4-GFP foci to Pbp1-mRuby foci in WT and *ado1Δ* strains. Bar graphs in A–C, E, G, I, and K are presented as average ± SEM of three independent replicates. Scale bars in D, E, H, and J are 5 µM. Statistical significance in E was determined by one-tailed paired Student's *t* test (*, P < 0.05).

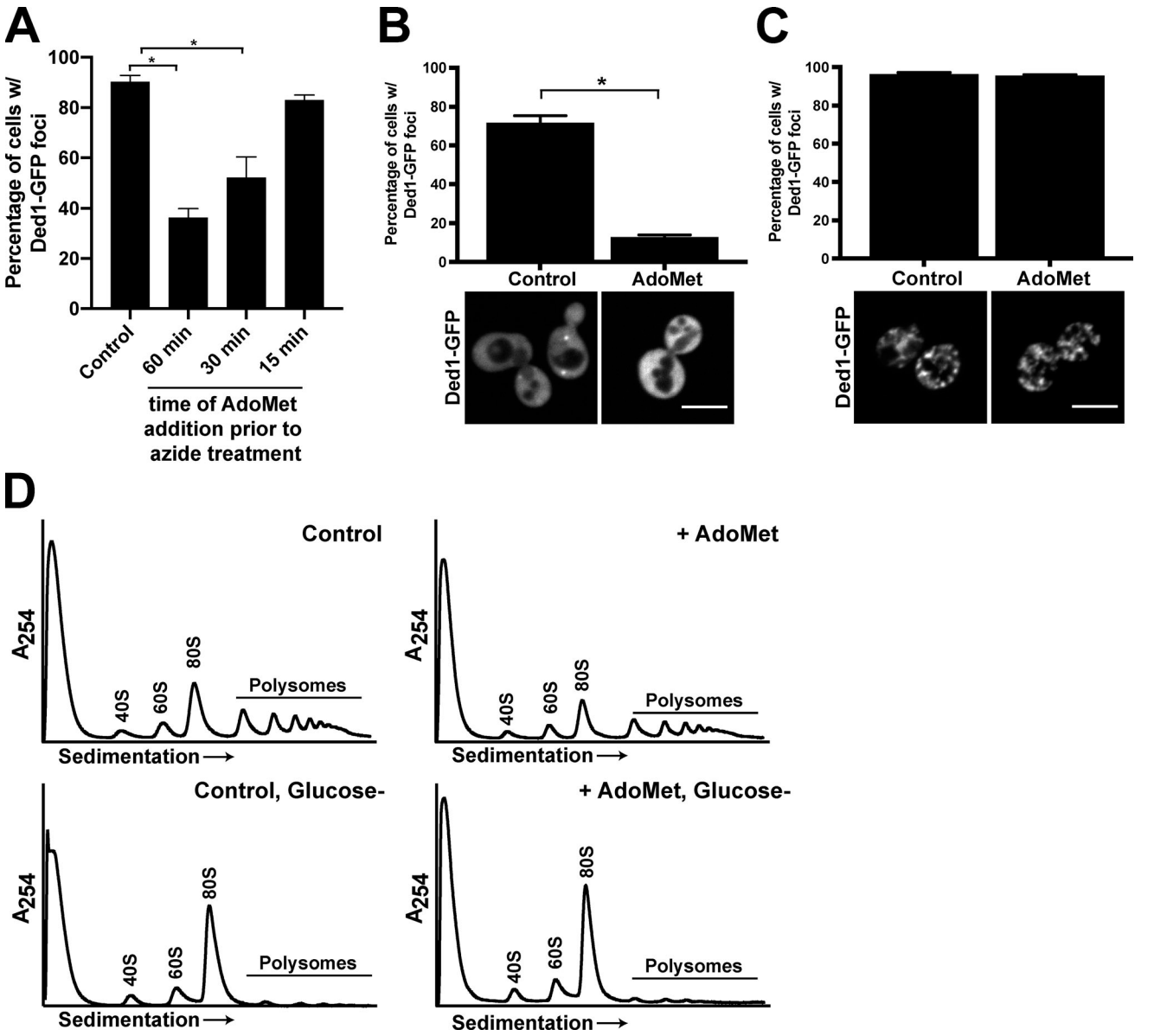

Figure S4. **Stress-specific and time-dependent effects of AdoMet treatment on acute-induced SG formation in yeast. (A)** Quantification of azide-induced SG formation in non–AdoMet-treated cells (Control) or cells treated with 250 µM AdoMet at the indicated time point before azide addition. **(B)** Quantification and representative fluorescent images of logarithmically growing with (AdoMet) or without (Control) 250 µM AdoMet strains expressing Ded1-GFP upon glucose deprivation. **(C)** Quantification and representative fluorescent images of logarithmically growing with (AdoMet) or without (Control) 250 µM AdoMet strains expressing Ded1-GFP upon heat shock. **(D)** Polysome traces from logarithmically growing strains with or without 250 µM AdoMet under unstressed or glucose deprived (Glucose–) conditions. Bar graphs in A–C presented as average ± SEM of three independent replicates. Scale bars in A and B are 5 µM. Statistical significance in A and B was determined by one-tailed paired Student's *t* test (*, $P < 0.05$).

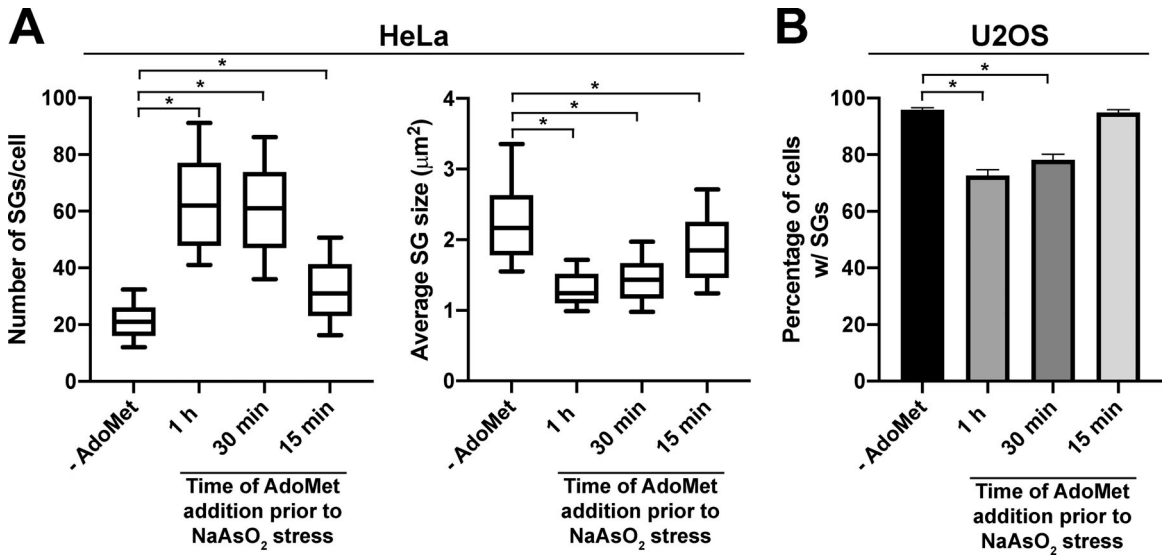

Figure S5. **Time-dependent effects of AdoMet treatment on arsenite-induced SG formation in mammalian cells. (A)** Box plots displaying quantification of number of SGs/cell and average SG size of HeLa cells treated with or without 4 mM AdoMet at the indicated time point before 500 µM $NaAsO_2$ for 1 h. Box plots represent a compilation of three independent experiments. **(B)** Quantification of U2OS cells containing SGs treated with or without 4 mM AdoMet at the indicated time point before 500 µM $NaAsO_2$ for 1 h. Data are presented as average ± SEM of three independent replicates. In A, statistical significance was determined by one-tailed unpaired Student's *t* test, and in B, one-tailed paired Student's *t* test (*, $P < 0.05$). For box plots, the ends of the box mark the 25th and 75th percentiles. The median is marked by a horizontal line inside the box. The whiskers mark the minimum and maximum measurements.

Five tables are provided online. Table S1 shows colocalization analysis of hits from RNA granule screen. Table S2 shows domain analysis of hits from RNA granule screen. Table S3 shows domain analysis of non-hits from RNA granule screen. Table S4 lists yeast strains used in this study. Table S5 lists the oligonucleotides used in this study.